

Air Force Institute of Technology

AFIT Scholar

Theses and Dissertations

Student Graduate Works

3-26-2015

Scaling of an Optically Pumped Mid-Infrared Rubidium Laser

Paul J. Moran

Follow this and additional works at: <https://scholar.afit.edu/etd>



Part of the [Engineering Physics Commons](#)

Recommended Citation

Moran, Paul J., "Scaling of an Optically Pumped Mid-Infrared Rubidium Laser" (2015). *Theses and Dissertations*. 88.

<https://scholar.afit.edu/etd/88>

This Thesis is brought to you for free and open access by the Student Graduate Works at AFIT Scholar. It has been accepted for inclusion in Theses and Dissertations by an authorized administrator of AFIT Scholar. For more information, please contact AFIT.ENWL.Repository@us.af.mil.



SCALING OF AN OPTICALLY PUMPED MID-INFRARED RUBIDIUM LASER

THESIS

PAUL J. MORAN, 2D LT, USAF

AFIT-ENP-MS-15-M-104

DEPARTMENT OF THE AIR FORCE

AIR UNIVERSITY

AIR FORCE INSTITUTE OF TECHNOLOGY

Wright-Patterson Air Force Base, Ohio

DISTRIBUTION STATEMENT A. APPROVED FOR PUBLIC RELEASE;
DISTRIBUTION IS UNLIMITED.

The view expressed in this thesis are those of the author and do not reflect the official policy or position of the United States Air Force, Department of Defense, or the U.S. Government.

AFIT-ENP-MS-15-M-104

SCALING OF AN OPTICALLY PUMPED MID-INFRARED RUBIDIUM LASER

THESIS

Presented to the Faculty

Department of Engineering Physics

Graduate School of Engineering Management

Air Force Institute of Technology

Air University

Air Education and Training Command

In Partial Fulfillment of the Requirements for the

Degree of Master of Science in Applied Physics

Paul J. Moran, B.S.

2d Lt, USAF

March, 2015

DISTRIBUTION STATEMENT A. APPROVED FOR PUBLIC RELEASE;
DISTRIBUTION IS UNLIMITED.

SCALING OF AN OPTICALLY PUMPED MID-INFRARED RUBIDIUM LASER

Paul J. Moran, B.S.

2nd Lt, USAF

Committee Membership

Glen P. Perram, Ph.D.
Chair

Christopher A. Rice, Ph.D.
Member

John R. Bruzzese, Ph.D.
Member

Abstract

An optically pumped mid-infrared rubidium (Rb) pulsed laser has been demonstrated in a heat pipe along both the $6^2P_{3/2} - 6^2S_{1/2}$ transition at 2.730 μm and the $6^2P_{1/2} - 6^2S_{1/2}$ transition at 2.790 μm . The bleached limit, slope efficiency, and maximum laser output energy of the mid-IR Rb laser have been shown to scale linearly with increasing Rb density, contrary to prior laser demonstrations. A maximum output energy of ~ 5 nJ per pulse had previously been observed before a rollover occurred in the scaling of output energy with Rb concentration. In this experiment, the maximum laser output energy observed was ~ 100 nJ, with linear scaling to a rubidium concentration of $7 \times 10^{15} \text{ cm}^{-3}$. A maximum slope efficiency based on incident pump photons of 1.7×10^{-4} was observed. Evidence that only a small percentage ($< 2\%$) of the available pump photons were absorbed at a concentration of $2 \times 10^{15} \text{ cm}^{-3}$ and a pump energy of 10 μJ . This indicated that there were $\sim 20,000$ pump photons per Rb atom at a pump energy of 10 mJ, and that the effective laser efficiency was 0.65% or higher. The hyperfine structure and absorption spectral profile of the $5^2S_{1/2} - 6^2P_{1/2}$ and $5^2S_{1/2} - 6^2P_{3/2}$ (blue) pump transitions were studied using a continuous wave (cw) pump source.

Acknowledgments

I would like to thank Dr. Glen Perram for his guidance in conducting this research. I would like to especially thank Dr. Christopher Rice for countless hours of help in the lab and in conducting data analysis; without him, this work would not have been possible. I would also like to thank Dr. John Bruzzese, Mike Ranft, Greg Smith, and Dr. Jamie Williamson for their help throughout the completion of this thesis, as well as fellow students James Rosenthal, Woody Miller, and Ben Eshel for their assistance and advice. I would like to thank my family for their support throughout the completion of this thesis.

Table of Contents

	Page
Abstract	v
Acknowledgements	vi
Table of Contents	vii
List of Figures	ix
List of Tables	xi
I. Introduction	1
II. Background	5
Chapter Overview.....	5
Theory	5
Background	8
III. Experiment.....	11
Chapter Overview.....	11
Experimental Setup	11
Calibration	17
Blackbody Calibration.....	17
Daylight Solutions Calibration.....	19
IR Spot Size and Beam Divergence	21
Laser Excitation Spectra and Measurement of Saturation Broadening.....	22
Rb Laser Output Energy vs. Pump Energy	22
Rb Laser Output Energy vs. Rb Concentration	23
Pulsed Absorption Spectra	23
Continuous Wave (cw) Diode Pump Experiments.....	25
IV. Results.....	27
Chapter Overview.....	27
Beam Shape	27
Laser Excitation Spectra.....	31
Rb Laser Output Energy vs. Pump Energy	35
Rb Laser Output Energy vs. Rb Concentration	44

Pulsed Absorption Spectra and Laser Efficiency	46
Continuous Wave (cw) Absorption Spectra and cw Laser Attempt	50
Assumptions, Error, and Uncertainty	57
V. Conclusion	59
Conclusions and Discussion	59
Recommendations for Future Work	61
Bibliography	63
Appendix	65

List of Figures

	Page
Figure 1.1. IR Pulse Energy vs. Rb Concentration (Richards, 2013:29)	2
Figure 2.1. Energy Level Diagram for Rubidium.....	5
Figure 3.1. Experimental Setup	11
Figure 3.2. Heat Pipe Assembly	12
Figure 3.3. Rb Number Density vs. Heat Pipe Temperature	14
Figure 3.4. Sample Trace of Laser Decay.....	16
Figure 3.5. Blackbody Calibration Curve	18
Figure 3.6. Daylight Solutions Laser Calibration Curve	20
Figure 3.7. Pulsed Absorption Spectroscopy Setup.....	24
Figure 3.8. Continuous Wave Absorption Spectroscopy Setup.....	25
Figure 3.9. Setup for Attempted cw IR Laser	26
Figure 4.1. Pump Beam Shape.....	27
Figure 4.2. Pump Beam Shape with Increasing Attenuation	28
Figure 4.3. IR Beam Shape	29
Figure 4.4. Laser Excitation Spectra.....	32
Figure 4.5. Effect of Saturation Broadening	34
Figure 4.6. Output Energy vs. Pump Energy ($6^2P_{3/2}$ - $6^2S_{1/2}$ transition)	36
Figure 4.7. Output Energy vs. Pump Energy ($6^2P_{1/2}$ - $6^2S_{1/2}$ transition)	37
Figure 4.8. Output Energy vs. Pump Energy ($6^2P_{3/2}$ - $6^2S_{1/2}$) (Richards, 2013:24)	38
Figure 4.9. Output Energy vs. Pump Energy ($6^2P_{1/2}$ - $6^2S_{1/2}$) (Richards, 2013:25)	39
Figure 4.10. Bleached Limit vs. Rb Concentration	40
Figure 4.11. Slope Efficiency vs. Rb Concentration	42
Figure 4.12. Threshold Pump Energy vs. Rb Concentration	43
Figure 4.13. Laser Output Energy vs. Rb Concentration.....	44
Figure 4.14. Pulsed Absorption Spectra	47
Figure 4.15. cw Absorption Spectra for the $5^2S_{1/2}$ - $6^2P_{1/2}$ (421.7 nm) Pump Transition	51
Figure 4.16. cw Absorption Spectra for the $5^2S_{3/2}$ - $6^2P_{1/2}$ (420.2 nm) Pump Transition	52
Figure 4.17. Peak Absorbance vs. Rb Concentration ($5^2S_{1/2}$ - $6^2P_{1/2}$ transition)	53

Figure 4.18. Theoretical vs. Experimental Peak A_{peak} ($5^2S_{1/2}$ - $6^2P_{1/2}$ transition).....	54
Figure 4.19. Ratio of Theoretical to Experimental A_{peak} vs. Rb Concentration.....	56
Figure A.1. Bleached Limit vs. Rb Concentration (Richards, 2013:27).....	65
Figure A.2. Slope Efficiency vs. Rb Concentration (Richards, 2013:27).....	66
Figure A.3. Blackbody Calibration Curve (Richards, 2013:18)	67
Figure A.4. InSb Peak-to-Peak Voltage Received	68

List of Tables

	Page
Table 2.1. Fundamental Constants.....	6
Table 2.2. A Coefficients, Cross Sections, and Energy Differences	7
Table 4.1. IR Beam Shape Fit Parameters	30
Table 4.2. Laser Excitation Spectra Fit Parameters	33
Table 4.3. Saturation Broadening Fit Parameters	34
Table 4.4. Energy Scaling Fit Parameters.....	37
Table A.1. Verification of Attenuation Factors of OD-0.5 ND Filter	69
Table A.2. Verification of Attenuation Factors of OD-1.0 ND Filter	69
Table A.3. Verification of Attenuation Factors of OD-2.0 ND Filter	69

SCALING OF AN OPTICALLY PUMPED MID-INFRARED RUBIDIUM LASER

I. Introduction

Diode Pumped Alkali Lasers (DPAL), first demonstrated by Krupke in 2003 (Krupke, 2003:2337), are simple and efficient lasers that have significant potential for use as directed energy weapons (Pandev, 2012). The use of DPALs for defense applications is desirable due to their high quantum efficiency, good beam quality, small thermal effect compared to other laser systems, and ability to be scaled to high power ($> 1\text{ kW}$) (Krupke, 2008).

Many Air Force directed energy programs, most notably the counter-ICBM mission, require the additional stipulation that the laser operates at a wavelength with a high degree of atmospheric transmission so that laser power is not absorbed or scattered over large distances (Tsipis, 1981:53). The infrared countermeasure (IR-CM) mission also requires output further into the IR ($>1\text{ }\mu\text{m}$) than the output of the standard rubidium (Rb) DPAL of 794.5 nm. An alternative laser scheme could use the DPAL concept to produce a mid-infrared rubidium laser at $2.7\text{ }\mu\text{m}$, where atmospheric transmission is superb (Traub, 1976:369). Such a laser is demonstrated here. By pumping to the $6^2\text{P}_{3/2}$ and $6^2\text{P}_{1/2}$ excited states of Rb at 420.2 and 421.1 nm (blue) respectively, laser action can be achieved along the $6^2\text{P}_{3/2} - 6^2\text{S}_{1/2}$ and $6^2\text{P}_{1/2} - 6^2\text{S}_{1/2}$ transitions at 2.730 and $2.790\text{ }\mu\text{m}$.

Optically pumped $6^2\text{P}_{3/2} - 6^2\text{S}_{1/2}$ and $6^2\text{P}_{1/2} - 6^2\text{S}_{1/2}$ Rb lasing has been demonstrated in the past on two occasions. Sharma demonstrated a continuous wave (cw) mid-IR Rb laser in 1981 (Sharma, 1981:209), and Richards demonstrated mid-IR Rb lasing using a pulsed pump in 2013 (Richards, 2013:1). However, both of these attempts achieved maximum slope efficiencies of only $\sim 10^{-6} - 10^{-5}$, with pump energies near 1 mJ and maximum outputs of about 5 nJ (Richards, 2013:23-

25). Additionally, both observed a rollover in output energy scaling as a function of increased Rb density beyond $n \sim 2.5 \times 10^{14} \text{ cm}^{-3}$ (Richards, 2013:29). Both of these trends can be seen in Figure 1.1, a figure produced by Richards of his Rb concentration scaling data overlaid with Sharma's.

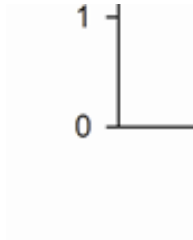


Figure 1.1. Figure from Richards showing output energy as a function of Rb concentration. The black (●) and white (○) circles represent the 2.73 μm and 2.79 μm transitions from Richards' experiment. The solid line (—) represents the data from Sharma (scaled to match Richards' path length). This figure shows that at an Rb concentration of $\sim 2.5 \times 10^{14} \text{ cm}^{-3}$, both Richards and Sharma observed a rollover in IR laser output energy, at a maximum value measured by Richards of $\sim 5 \text{ nJ}$ (Richards, 2013:29).

Because of these results, both Sharma and Richards concluded that this laser could not be scaled to energies required for defense purposes. Sharma attributed the rollover in output power

and small efficiency to second-order quantum processes (Lucatorto, 1980:3948), with which Richards agreed. However, this thesis will show that the low efficiency and scaling rollover reported by both Richards and Sharma was a not due to the physics of the laser mechanism, but was instead the product of experimental design.

Sharma's experiment, which used a 200-300 mW continuous wave (cw) pump source, was a single-pass laser with no optical resonator or collecting optics and an effective gain path length of 2.5 cm (Sharma, 1981:209). Therefore, beam divergence was inversely related to the effective gain path length of the optical cavity. Since the laser power was held constant over the course of the experiment (Sharma, 1981:210), the output energy grew with increasing Rb concentration until the cell was perfectly bleached. This occurred near the rollover point shown in Figure 1.1. Beyond this point, the pump beam would have only penetrated an increasingly smaller percentage of the cell before all of the pump photons were absorbed. As a result, the effective gain path length would have shrunk, increasing the beam divergence as more Rb atoms were added. Thus, as Rb concentration increased, the detector would have received an increasingly smaller percentage of the output photons. This gave the appearance that the energy of the mid-IR Rb laser was decreasing with added Rb concentration.

Richards' experiment used a maximum 10 mJ pulsed pump source with a mirrorless cavity (Richards, 2013:11). Like Sharma, Richards observed a linear increase in output energy as a function of Rb concentration until $n \sim 2.5 \times 10^{14} \text{ cm}^{-3}$. Richards also observed a rollover in this scaling curve at this point, but for a different reason. Because Richards' experiment was pulsed, and the instantaneous pump intensity was very large ($\sim \text{MW/cm}^2$) compared to the saturation intensity, the bleaching phenomenon that affected Sharma's cw experiment would not have been the cause of the rollover. Instead, Richards' results were limited by detector saturation. Richards'

detector had a very small maximum receivable power before it became saturated. The fact that Richards' data in Figure 1.1 roll over but do not decline like Sharma's support this hypothesis. If not for Sharma's results, Richards may have realized this, but since his data appeared to agree with Sharma's, Richards believed this trend to be real.

The purpose of this thesis was to reproduce the work of Richards, accounting for detector saturation with an appropriate attenuation scheme in order to determine the maximum attainable efficiency of the laser and accurately scale the effect of increasing pump energy and Rb concentration on laser output energy. Specifically, it was demonstrated that bleached limit, slope efficiency, and laser output energy scale linearly with increasing Rb density. Evidence that the laser could be scaled to significantly higher efficiencies than reported by Sharma or Richards was also observed. In addition, a tunable blue diode laser was used to study the absorption spectra of rubidium at the pump transitions, and an attempt was made to demonstrate a cw mid-IR Rb laser to reproduce the work of Sharma.

II. Background

Chapter Overview

In this chapter, relevant theory pertaining to this experiment is discussed. In addition, significant prior work contributing to the development of diode and optically pumped alkali lasers is summarized. The work of Sharma and Richards is examined in detail, as their experiments provide the basis for this thesis.

Theory

The energy level diagram for rubidium is shown in Figure 2.1.

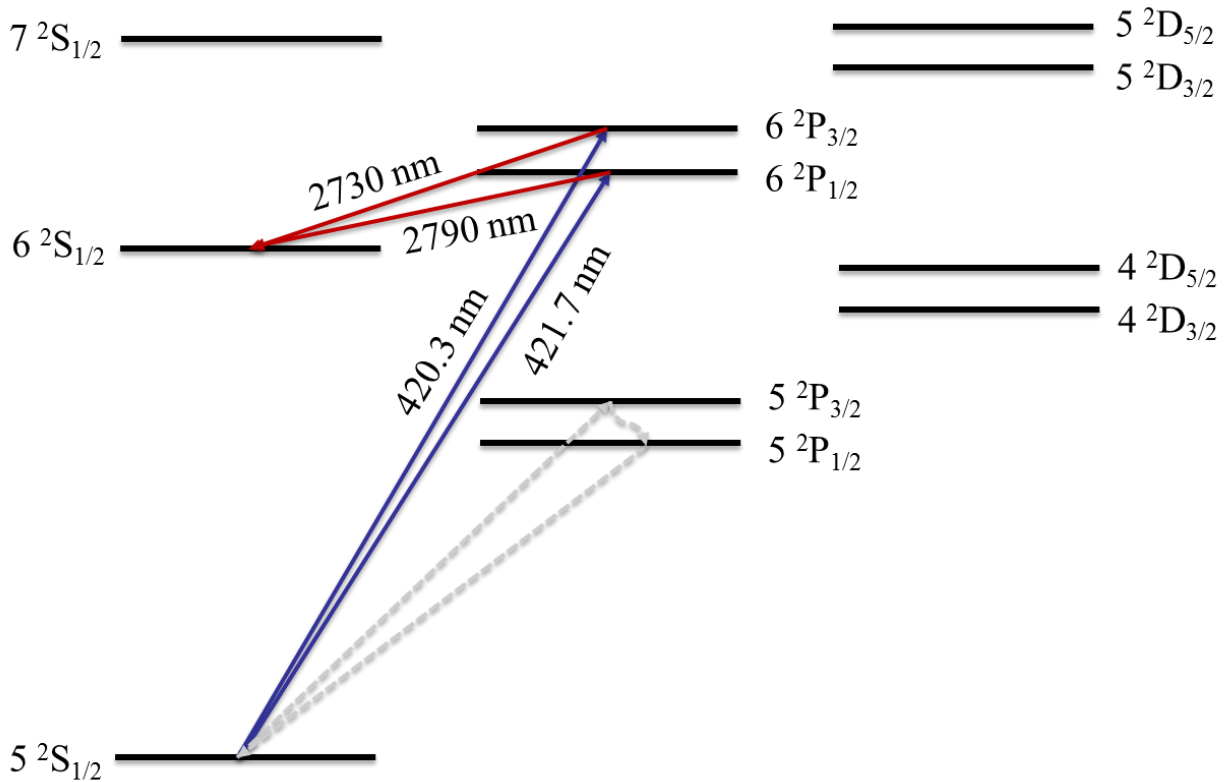


Figure 2.1. Energy level diagram for rubidium. The mid-IR Rb laser scheme is shown. Rb atoms are optically pumped from the ground state by a blue laser at 420.2 nm to the $6^2P_{3/2}$ state and at 421.7 nm to the $6^2P_{1/2}$ state. In both cases, lasing occurs directly to the $6^2S_{1/2}$ state at 2.730 μm and 2.790 μm , respectively. For reference, the typical Rb DPAL mechanism is shown in gray.

The typical Rb DPAL (shown in gray in Figure 2.1) operates by pumping from the ground state ($5^2S_{1/2}$) to the second excited state ($5^2P_{3/2}$) at 780 nm. Collisional relaxation moves population from the $5^2P_{3/2}$ state to the $5^2P_{1/2}$ state, and lasing occurs on the 794.5 nm ($5^2P_{1/2} - 5^2S_{1/2}$) D_1 transition. For the mid-IR Rb laser, pumping occurs from the ground state to the $6^2P_{3/2}$ or $6^2P_{1/2}$ states at wavelengths of 421.7 nm and 420.2 nm. Excited atoms in these states lase directly to the $6^2S_{1/2}$ state, with no need for spin-orbit relaxation as in the traditional DPAL. These lasing transitions occur at 2.730 nm and 2.790 nm (Krupke, 2003:2337).

Table 2.1: Fundamental Constants

Speed of Light, c	2.99792458×10^8 m/s
Planck Constant, h	$6.62606957 \times 10^{-34}$ J•s
Boltzmann Constant, k	$1.3806488 \times 10^{-23}$ J/K
Atomic Mass of Neutral Rubidium, m_{Rb}	85.4678 AMU
Index of Refraction in Air, n_{air}	1.000293

Several fundamental constants used in computations throughout the work presented here are provided in Table 2.1. In Table 2.2, Einstein A coefficients, stimulated emission cross sections, and energy differences are presented for the relevant Rb transitions of both the traditional DPAL and the blue-pumped mid-IR Rb laser. The stimulated emission cross section, σ_{ji} , for each transition was calculated using Equation 2.1,

$$\sigma_{ji} = \frac{A_{ji}\lambda_{ji}^2}{8\pi n^2} g(v_{ji}) , \quad (1)$$

where A_{ji} is the Einstein A coefficient, λ is the transition wavelength in air, n is the index of refraction in air, and $g(v_{ji})$ is the Doppler lineshape [Verdeyen, 1989]. As the cell was held at

vacuum, Doppler broadening was expected to dominate. The Doppler lineshape was calculated using Equation 2.2,

$$g(\nu) = \sqrt{\frac{4 \ln 2}{\pi}} \frac{1}{\Delta \nu_D} \exp\left[-4 \ln 2 \left(\frac{\nu - \nu_0}{\Delta \nu_D}\right)^2\right], \quad (2)$$

where ν is the frequency, ν_0 is the central frequency of the transition, and $\Delta \nu_D$ is the Doppler width, calculated using Equation 2.3,

$$\Delta \nu_D = \left(\frac{8kT \ln 2}{Mc^2}\right)^{1/2} \nu_0, \quad (3)$$

where k is the Boltzmann constant, T is the temperature, c is the speed of light, and M is the molecular mass of Rb in atomic mass units (AMU) [Verdeyen, 1989]. The Doppler width varied with temperature; at 160° C, the Doppler widths of the pump transitions were 1.14 GHz ($5^2S_{1/2}$ - $6^2P_{1/2}$) and 1.15 GHz ($5^2S_{1/2}$ - $6^2P_{3/2}$).

Table 2.2: A Coefficients, Cross Sections, and Energy Differences for Relevant Transitions

Transition	A Coefficient, A_{ji} (s^{-1})	Cross Section, σ_{ji} (cm^2)	Energy Difference, ΔE (cm^{-1})
$5^2S_{1/2}$ - $6^2P_{3/2}$	1.77×10^6	9.83×10^{-11}	23792.591
$5^2S_{1/2}$ - $6^2P_{1/2}$	1.50×10^6	2.52×10^{-11}	23715.081
$6^2P_{3/2}$ - $6^2S_{1/2}$	4.63×10^6	7.76×10^{-11}	3660.08
$6^2P_{1/2}$ - $6^2S_{1/2}$	4.40×10^6	7.91×10^{-11}	3582.57
$5^2P_{3/2}$ - $5^2S_{1/2}$	3.81×10^7	1.35×10^{-11}	12816.545
$5^2P_{1/2}$ - $5^2S_{1/2}$	3.61×10^7	1.40×10^{-11}	12578.95

Background

The concept of an optically pumped alkali laser was initially proposed by Schawlow and Townes (Schawlow, 1958:1840), as an expansion of the MASER (*Microwave Amplification of Stimulated Emission by Radiation*) first built by Townes, Gordon and Zeiger at Columbia University in 1953 (Gordon, 1954:283). As its name suggests, the original MASER was intended to amplify microwave radiation, but in their 1958 paper Schawlow and Townes considered a MASER operating in the optical, IR, and UV. They proposed the use of potassium (K) as a gain medium because it was easy to vaporize and had a simple spectrum. By pumping with a filtered potassium lamp at 404.7 nm, vaporous potassium atoms could be electrically excited from the ground state ($4^2S_{1/2}$) to the $5^2P_{3/2}$ and $5^2P_{1/2}$ excited states. With a sufficiently fast pump rate, they suggested that a population inversion in the 5p states could be achieved. This would potentially lead to MASER action from the 5p to the 5s or 3d states, at 2.71 μm and 3.14 μm respectively, in the mid-infrared. Schawlow and Townes named such a system the “optical MASER.”

Rabinowitz, along with Gould and Jacobs, realized the optically pumped alkali laser in 1962 (Rabinowitz, 1962:514) using cesium (Cs) as the gain medium. The laser was optically pumped by a He lamp at 388.8 nm, sufficient to excite Cs atoms from the ground state ($6^2S_{1/2}$) to the $8^2P_{1/2}$ state. Lasing occurred in the far-infrared, at 7180 nm. Rabinowitz used an optical resonator to amplify the continuous-wave (cw) laser light, achieving an output power of 25 μW .

Sorokin was the first to observe lasing in Rb, K and Cs using a pulsed source, achieving lasing at 2254 nm and 2293 nm in Rb (Sorokin, 1970:2930). A 500 mW ruby laser was used to pump vaporous alkali samples via two-photon absorption. Lasing occurred along the 6P-4D transition in Rb. Additionally, Sorokin’s work was one of the first experiments that used a heat pipe as the gain cell. This experiment would influence the work of Sharma (Sharma, 1981:210).

Krupke, et al produced the first DPAL systems in 2003, achieving laser action in vaporous rubidium, cesium, and potassium (Krupke, 2003:2337). Krupke used a tunable diode-pumped titanium-sapphire laser to pump vaporous alkali atoms from the ground state to the second excited ($^2P_{3/2}$) state. The lifetime of the laser transition was approximately 30 ns. Ethane gas was used to achieve rapid mixing of the $^2P_{3/2}$ and $^2P_{1/2}$ states. Helium was used as a buffer gas to ensure the absorption features of the alkalis were sufficiently broadened to accept a broad-band diode pump. Using this mechanism, Krupke demonstrated lasing at 770 nm (K), 795 nm (Rb), and 895 nm (Cs).

Sharma first demonstrated mirrorless cw lasing in the $6^2P_{3/2} - 6^2S_{1/2}$ and $6^2P_{1/2} - 6^2S_{1/2}$ transitions in rubidium, as well as corresponding $n = 7$ transitions in cesium (Sharma, 1981:209). Sharma used a 200-300 mW cw Ar^+ pump laser operating in the ultraviolet to pump a dye laser circulating Stilbene 3 dye. The dye laser was used to pump to the $7^2P_{1/2}$ and $7^2P_{3/2}$ states in Cs at 410 nm and 470 nm, and to the $6^2P_{1/2}$ and $6^2P_{3/2}$ states in Rb at 421.7 nm and 420.2 nm. Both Cs and Rb lased directly to the 7S and 6S first excited states, respectively, at 3.095 μm and 2.93 μm in Cs and 2.79 μm and 2.73 μm in Rb. The solid alkali samples were housed in a glass cell (Cs) and a glass bulb (Rb), and heated to temperatures up to 400° C. For both Cs and Rb, beyond a certain temperature (120° C for Rb, corresponding to a population density of $2.6 \times 10^{13} \text{ cm}^{-3}$, and 169° C for Cs, corresponding to a population density of $2.9 \times 10^{14} \text{ cm}^{-3}$) Sharma observed rollover and steep decline of stimulated emission intensity on the lasing transition. He attributed this to second ordered quantum processes, believing that atoms in the 6P states were excited to higher quantum states (e.g. 6D, 7D, 8S, 9S). Lucatorto and McIlrath proposed several mechanisms by which 6P Rb atoms could be excited to higher energy levels. These included photoionization of energy-pooled 6P Rb atoms (Lucatorto, 1976:428), auto-ionized dimer formation due to collisions between excited atoms (Bearman, 1978:1227), simultaneous pump photon absorption and collision

with an excited atom (Polak-Dingels, 1980:1663), and stimulated Raman scattering (Lucatorto, 1976:428).

In 2013, Richards expanded on the work of Sharma by demonstrating mirrorless lasing in the $6^2P_{3/2,1/2} - 6^2S_{1/2}$ transitions of optically pumped Rb with a pulsed pump source (Richards, 2013:11). Richards used a 10 ns pulsed, 1 MW/cm² Continuum neodymium-doped yttrium aluminum garnet (Nd:YAG) laser to pump at 1.06 μm . The wavelength was decreased to 355 nm by a frequency tripling crystal, sufficient to pump a Continuum 420 dye laser circulating Stilbene-4 (blue) dye. The dye laser was tunable over a range of 20 nm centered at 420 nm and was thus suitable to produce the pump transitions required. The pump beam was incident on a vaporous Rb sample contained in a heat pipe. The heat pipe was capable of heating the Rb sample to temperatures of 250° C. Like Sharma, Richards observed lasing at 2.79 μm and 2.73; also like Sharma, Richards saw rollover in stimulated emission intensity beyond a population density of approximately $2.5 \times 10^{14} \text{ cm}^{-3}$. Richards concluded that Sharma's prediction that maximum output energy and efficiency were limited by second order processes was correct. However, as mentioned in Chapter I, Richards' data was misinterpreted because of detector saturation. This is evident based on his blackbody calibration curve, shown in the Appendix (Figure A.3). The rollover in oscilloscope signal as function of radiometric power received by the detector is an indication of saturation. Richards incorrectly assumed that his data would fall on the linear portion of the blackbody calibration curve, leading to his observation of the rollover in his data in Figure 1.1.

The work of Richards was especially important to this thesis, as the primary goal of the work presented here was to investigate the conclusions of Richards' experiment. The lasing scheme and the majority of the experimental setup used were predominantly the same as those used by Richards, with several important changes that are discussed at length in Chapter III.

III. Experiment

Chapter Overview

In this chapter, parameters of the experimental setup are discussed. Topics covered include the experimental setup used to produce and characterize the mid-IR rubidium laser, the calibration scheme of the indium-antimonide (InSb) detector, and the setup of the cw experiments.

Experimental Setup

A schematic showing the optically pumped mid-IR Rb laser is shown in Figure 3.1.

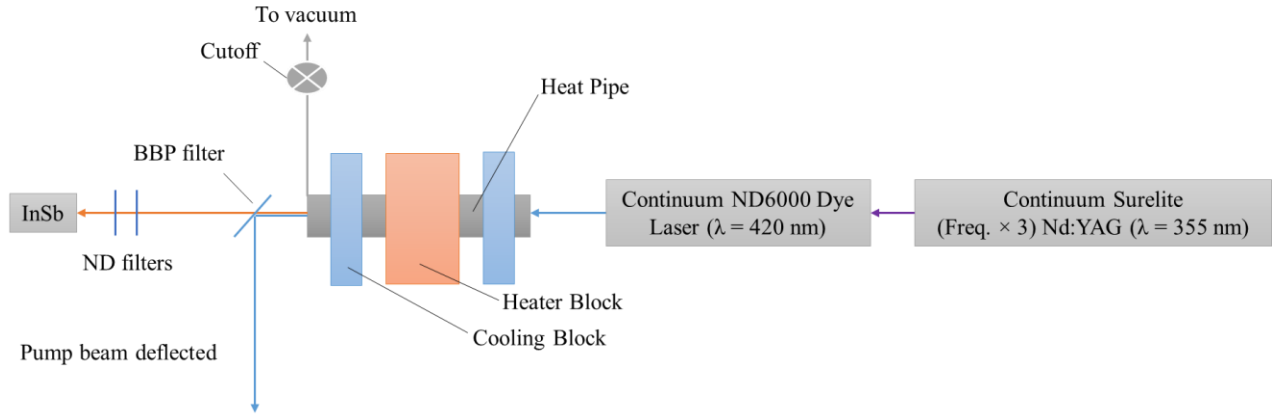


Figure 3.1. Experimental setup for all pulsed laser scaling experiments.

A Continuum Surelite frequency tripled ~ 1.8 GHz Nd:YAG laser pumped a 420 nm Continuum ND6000 dye laser circulating Stilbene 420 laser dye. The dye was tuned over the 421.7 nm $5^2S_{1/2} - 6^2P_{1/2}$ and 420.2 nm $5^2S_{1/2} - 6^2P_{3/2}$ transitions. The dye laser could provide pump energies of up to 14 mJ/pulse, with a 7 ns pulse lifetime at a repetition rate of 10 Hz. The maximum pump energy of 14 mJ/pulse was far larger than the bleached limit of the infrared Rb laser, even at the highest Rb concentration the heat pipe could attain. Additionally, the beam quality of the

blue pump beam was poor (see Figures 4.1 and 4.2), which made calculations of the pump active area and the number of photons per pump pulse difficult. Further discussion of the impact of beam quality on these experiments follows in Chapter IV.

The output beam of the dye laser was incident on the heat pipe assembly. A diagram of the heat pipe is shown in Figure 3.2.

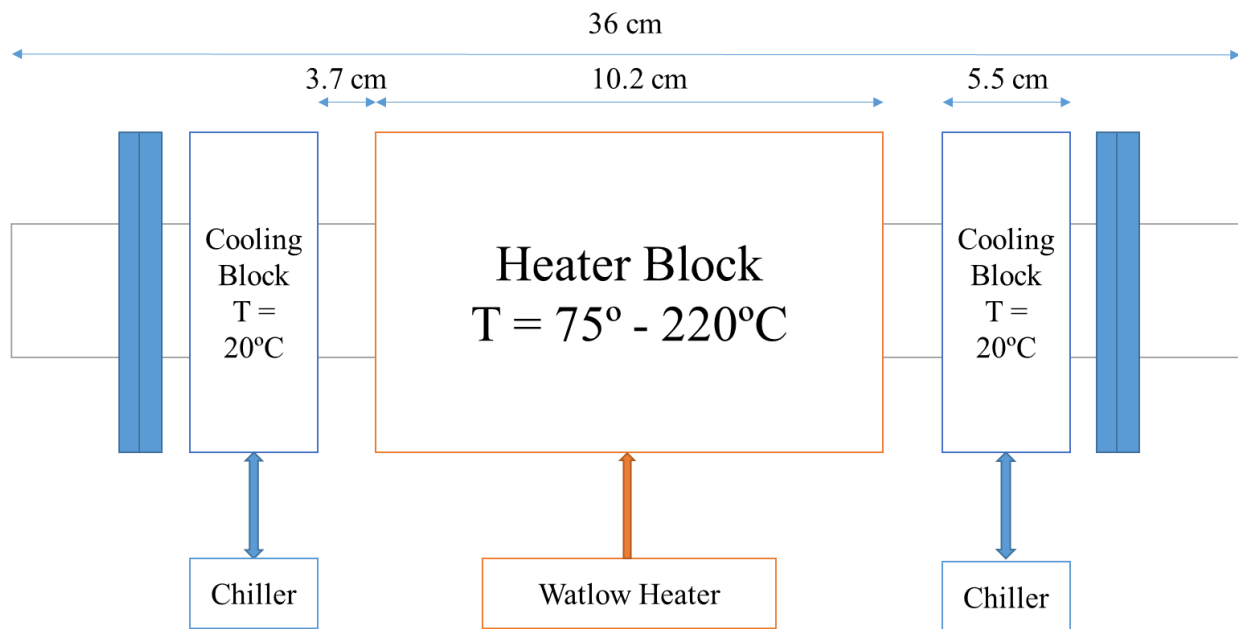


Figure 3.2. Heat pipe assembly.

The heat pipe consisted of a 36 cm long, 2 cm outer diameter stainless steel tube containing a 1 g sample of rubidium. In the center was a 10.2 cm heater block, connected to a thermocouple and eight Watlow heater plugs (model number C1E14-L12H), capable of heating the Rb sample to 220°C . 3.7 cm from either end of the heater block were two cooling blocks, through which a Neslab RTE-111 chiller circulated water at 20°C . Unlike a glass cell, in which the gain path length can be measured directly, the gain path length in a heat pipe must be approximated. The gain path length was taken to the length of the heater block (10.2 cm), although it is possible that the gain

region could have extended past the heater block and approached the cooling blocks. This gave an upper bound on the gain path length of ~ 18 cm. This large uncertainty had an impact on several calculations, including the number of excitable Rb atoms in the active volume and the absorption in the cell. This is discussed further in Chapter IV.

The heat pipe had several advantages over other gain cell types, including that a constant Rb vapor concentration could be maintained (compared to a glass cell, where population density can vary spatially across the beam path), and that a higher temperature (and therefore higher Rb concentration) could be reached than in a pyrex cell. This was done by the following mechanism. Hot vaporous Rb atoms at the center of the heat pipe traveled via temperature gradient toward the cold region. When the vapor reached the chillers, it condensed, and the liquid traveled back toward the heated region by capillary action along a 150×150 wire/inch stainless steel mesh. The Rb sample was heated to temperatures from 75° to 220° Celsius. These temperatures were converted to Rb number density using vapor pressure, related to temperature by Equation 3.1:

$$\text{Log}_{10}(P_v) = 2.881 + 4.312 - \frac{4040}{T}, \quad (1)$$

where P_v is the vapor pressure in Torr, and T is the temperature in Kelvin (Steck, 2008:3). The number density in the cell was then calculated from the ideal gas law, $PV = NkT$, where k is the Boltzmann constant. The number density $n = N/V$ of Rb atoms in the heat pipe ranged from $1.08 \times 10^{12} \text{ cm}^{-3}$ at 75° C to $1.96 \times 10^{15} \text{ cm}^{-3}$ at 220° C . Equation 3.1 and the ideal gas law were used to produce the Rb number density vs temperature curve shown in Figure 3.3.

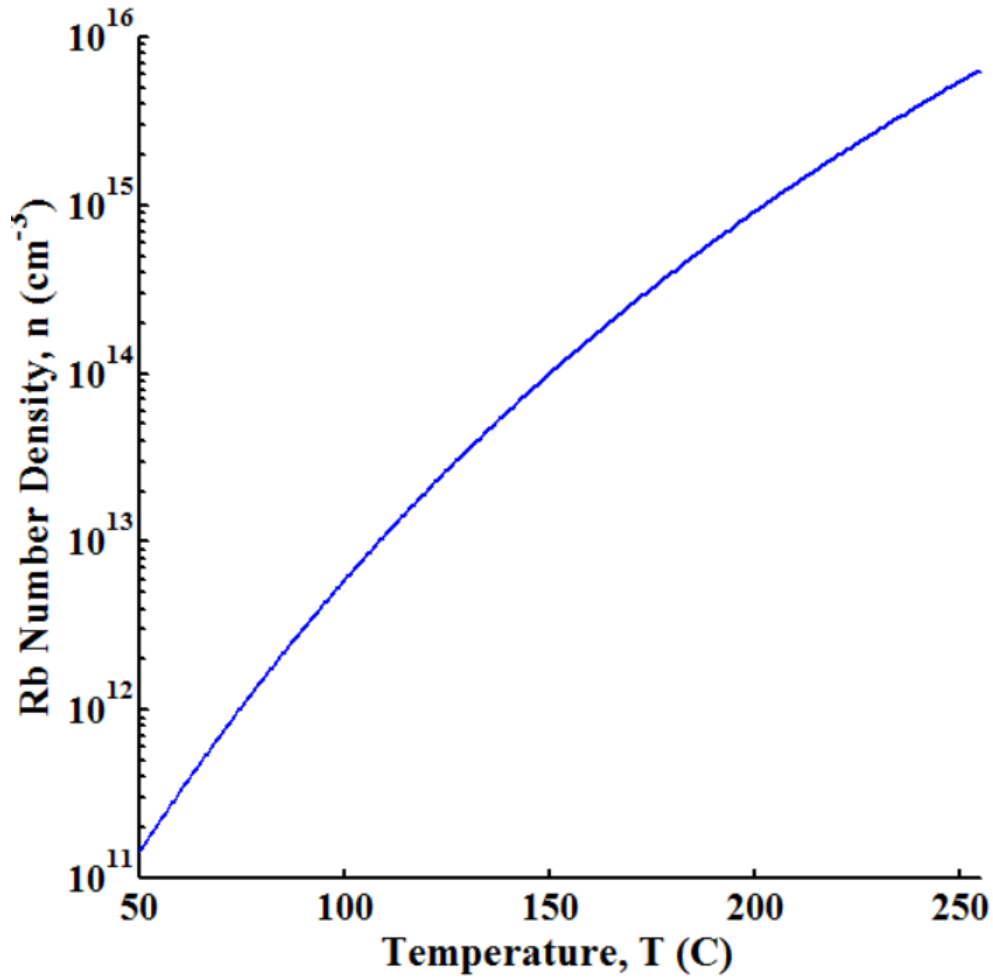


Figure 3.3. Rb number density as a function of heat pipe temperature. At the maximum temperature of the heat pipe (220° C) the vapor pressure of the cell was 100.17 mTorr. The number density $n = N/V$ was found from the vapor pressure and the temperature of the cell using the ideal gas law. The maximum Rb number density was $\sim 2 \times 10^{15} \text{ cm}^{-3}$.

From the Rb number density, the active volume of the heat pipe could be found given the approximate gain path length and the beam spot area. The active volume was an important parameter to understand when considering the scaling and efficiency of the laser. See the section in Chapter IV on Beam Shape for an estimation of the active volume.

On either end of the heat pipe were 5 mm-thick, uncoated fused silica windows which passed both the pump and Rb beams. The fused silica windows were used for nearly all

experiments using the dye laser as a pump source. They were later changed to sapphire windows in an attempt to improve transmission of the IR beam. However, after the windows were scanned with a monochromator, the transmission at 2.79 and 2.73 μm was actually found to be worse for the sapphire windows (~74%) than for the fused silica windows (~86%). The fused silica windows were used for all pulsed case results presented in Chapter IV. The sapphire windows were used for the cw experiments.

The beam exiting the heat pipe consisted of the combined mid-IR beam and the pump beam. To separate the blue pump, a ThorLabs broad band pass filter centered at 2.75 μm with a FWHM of 0.5 μm was placed immediately after the exit window of the heat pipe.

In Richards' experiment, the separated IR beam was then incident on a liquid nitrogen cooled indium antimonide (InSb) detector (Richards, 2013:11). As mentioned previously, Richards' data and conclusions were impacted by detector saturation. Therefore, the setup used by Richards was modified by placing two neutral density (ND) filters in front of the InSb detector. The combination of a Newport mid-IR reflective OD-2.0 ND filter and a Thor Labs absorptive OD-0.5 ND filter attenuated the beam by a factor of approximately 500 (verified by experiment; see Appendix), sufficient to provide an unsaturated signal even at the highest IR laser energies measured.

The detector used in this experiment was a liquid nitrogen-cooled, Teledyne Judson J10D photovoltaic InSb detector with an active area of 0.01 mm². The detector was connected to a Perry Amplifier pre-amplifier with a 7 ns rise time that was custom matched to the InSb. The response time of the pre-amp was slow compared to the detector response time, leading to the ringing seen in Figure 3.4. Assuming the detector was unsaturated, the detector should have given a linear mapping from area (V·s) of the pulse decay curve to the power received by the detector. If true,

the ringing would be averaged out when integrating over the entirety of the pulse decay curve. The linearity of the calibration curves shown in Figures 3.5 and 3.6 indicates that this assumption was valid.

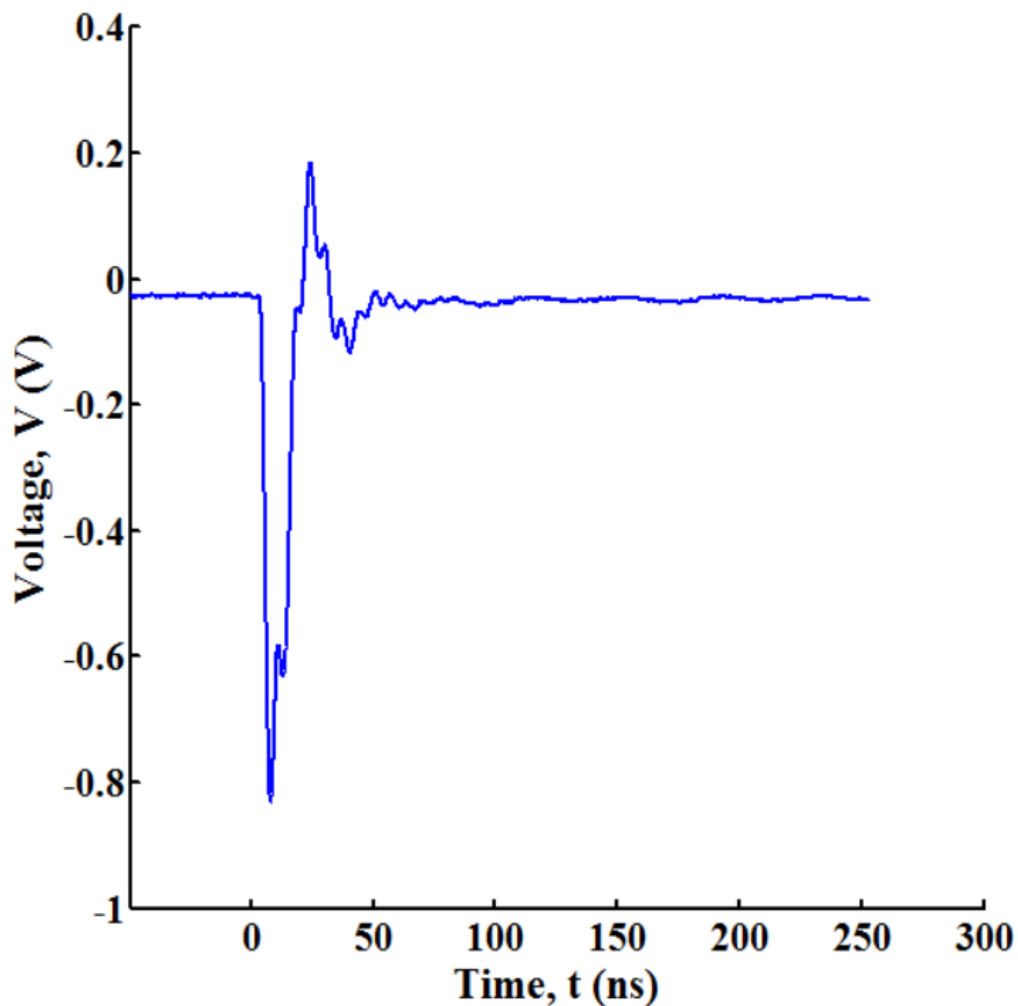


Figure 3.4. Sample trace of a laser decay curve showing ringing due to the slow response time of the Perry Amplifier pre-amp compared to the pulse lifetime. If the response time of the pre-amp were on the order of the laser pulse lifetime, the pulse would appear as an exponential decay.

The pre-amp was connected to an Agilent E3631A DC power supply, which supplied 5.00 V at 0.022 A, and a LeCroy WavePro 7100 1 GHz oscilloscope. The oscilloscope was used to save time-averaged traces of the pulse decay curves. The area of the IR laser pulse ($\text{V}\cdot\text{s}$) was converted to energy per pulse (J) by the method discussed in the following section.

Calibration

Initially, the conversion from voltage received by the detector to laser output energy was done using a blackbody calibration. Due to the significant impact of uncertainty in Richards' calibration on his results, a second method of calibration was sought. A Daylight Solutions mid-IR diode laser with a known output power was also used to calibrate the InSb detector, which proved to be a simpler method with fewer assumptions. Both methods are described below.

Blackbody Calibration

An Electro Optics Industries LDS1250-100 variable aperture blackbody was used for the blackbody calibration. A 1.01 kHz chopper was placed between the blackbody and the detector to remove background signal. By measuring the voltage difference (peak-to-peak) between the blocked and unblocked signals, the signal due solely to the blackbody could be determined. An example of a peak-to-peak voltage measurement is shown in the Appendix (Figure A.4).

To develop a response curve, the temperature, aperture size, and distance of the detector from the blackbody were varied. Temperature was varied from 400° to 1200° C in 100° increments. Aperture radii of 1.60 cm and 1.01 cm were used, and the detector was placed at distances of 15 cm, 17.5 cm, and 20 cm from the blackbody. The corresponding radiometric power at the detector for each iteration was calculated by Equation 3.2:

$$P = \int_{2 \mu m}^{5.25 \mu m} \left(\frac{A_s A_d}{\pi R^2} \right) \left(\frac{2hc^2}{\lambda^5 \left(e^{hc/\lambda kT} - 1 \right)} \right) d\lambda, \quad (2)$$

where P is the power received by the detector (in Watts), A_s is the area of the blackbody aperture, A_d is the active area of the detector, R is the distance from the blackbody aperture to the detector,

h is the Planck constant, k is the Boltzmann constant, c is the speed of light, and λ is wavelength (Dereniak, 1996). The wavelength was integrated over the detector response range, 2 to 5.25 μm . The resulting plot of oscilloscope signal (mV) vs. power received by the detector (nW) is shown in Figure 3.5.

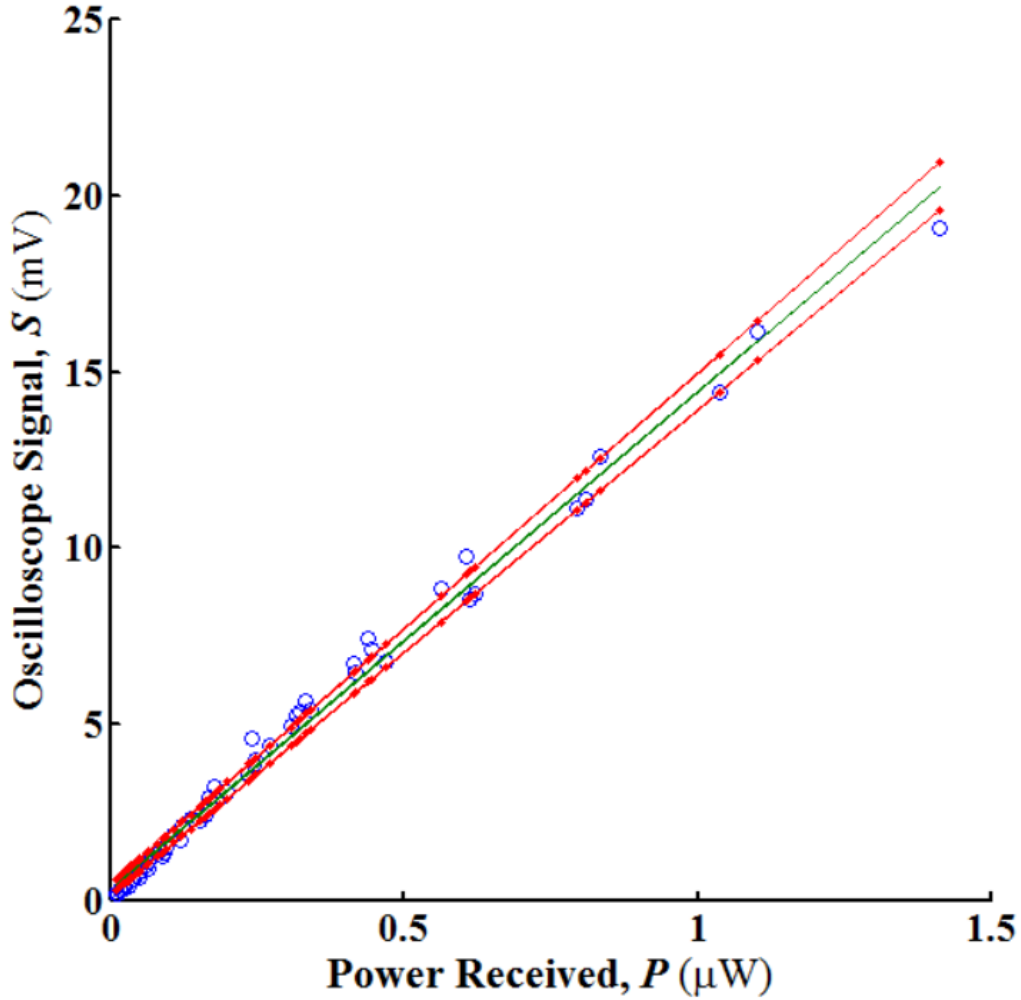


Figure 3.5. Blackbody calibration curve. Signal measured by the oscilloscope (mV) is plotted against power received by the detector (nW). The slope of the fit line (—) is 14.4 mV/ μW . The red lines give the 95 percent confidence intervals. The fit equation is 14.4 ± 0.72 mV/ μW .

The equation of the fit line was y (mV) = $14.4x$ (μW) + 0.32. The slope of the line, 14.4 ± 0.72 mV/ μW , was used as part of the conversion from the signal measured by the detector to the output energy of the laser. This was done as follows. The area of the pulse decay curve (V•s)

was converted to energy (J) by multiplying by slope of the calibration curve (V:W) and multiplying through by seconds ($1 \text{ J} = 1 \text{ W/s}$). The calculated energy was then multiplied by the experimentally verified attenuation factor of 481.5 ± 24.1 , in reasonable agreement with the factor of 500 expected based on the order of attenuation of the two ND filters. Experimentally determined losses at the rear window of the heat pipe (85.3 percent transmission) and the broad bandpass filter (76 percent transmission) were then accounted for. Lastly, the energy needed to be multiplied by the ratio of the detector active area to the laser spot size. The detector area (0.01 mm^2) was small compared to the laser spot ($\geq 1 \text{ mm}^2$), so only a small percentage of the total energy was received. However, determining this ratio was difficult. As discussed at length in Chapter IV, misalignment in the Continuum ND6000 dye laser led to poor beam quality, making the spot area of the pump beam difficult to measure accurately (see Figure 4.2). The infrared laser spot area was likewise difficult to determine. Based on experimental measurements (see Chapter IV), the IR laser spot area was conservatively taken to be 2.35 mm^2 . This gave a ratio of spot area to detector area of 235:1. Accounting for all these factors, the pulse area in Figure 3.4 of $4.5 \times 10^{-9} \text{ V}\cdot\text{s}$ gave $E_{out} = 54.29 \text{ nJ}$.

Daylight Solutions Calibration

As discussed above, the major impact of calibration on Richards' results led to the emphasis in this thesis on accurate calibration. The numerous assumptions involved in the blackbody calibration scheme made finding an alternate method desirable. There were many variables involved in the calculation of radiometric power, each of which introduced potential sources of error. Also, Equation 3.2 treats the responsivity of the detector as a step function, when in reality it is highly varied over the response range of the detector. Additionally, the accuracy of the blackbody's actual output compared to the theoretic radiometric power could not be confirmed.

For these reasons, a simpler calibration method was devised, using a cw IR laser with a known power as a function of input current.

A Daylight Solutions diode laser at $3.77\ \mu\text{m}$ with a maximum power of 72 mW was incident on the detector. In the beam path was a chopper rotating at 1 kHz and the same two ND filters used in all of the pulsed laser experiments. The peak-to-peak oscilloscope signal (mV) was found by the same method described for the blackbody calibration. By varying the power of the Daylight Solutions laser, a calibration curve was constructed. This is shown in Figure 3.6.

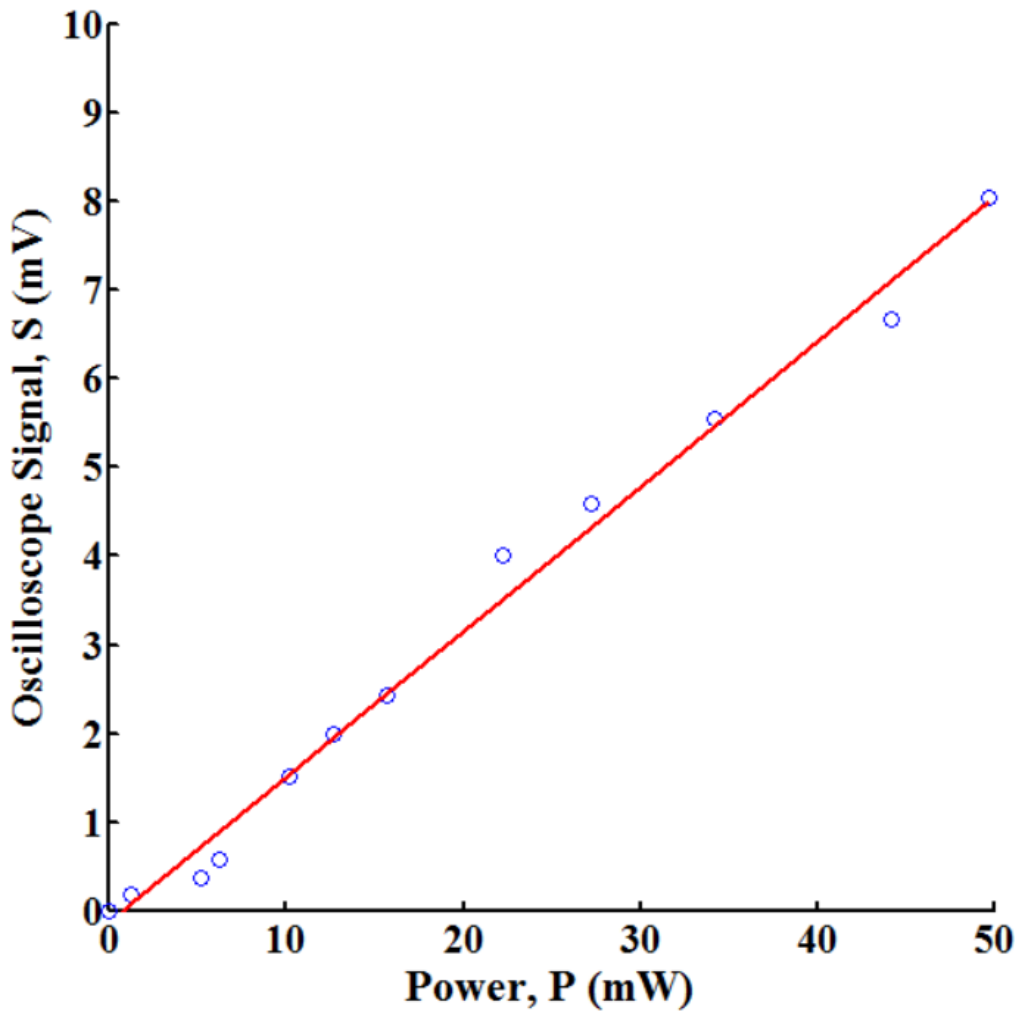


Figure 3.6. Oscilloscope signal (mV) vs. received power (mW) for the Daylight Solutions calibration. The slope of the fit line (—) is 0.144 mV/mW. The units differ by a factor of $\sim 10^3$ from the blackbody calibration. This is because the two ND filters described above were attached to the InSb detector in the Daylight Solutions calibration but not in the blackbody calibration.

The slope of the fit line, 0.144 mV/mW, gave the conversion from oscilloscope signal (mV) to power received (mW). As was done for the blackbody calibration, the area of the pulse decay curve (V•s) was converted to output energy by multiplying by the calibration factor and multiplying by seconds. Because the same ND filters were used for all pulsed experiments, the attenuation factor was built into the calibration. Thus the energy was not multiplied by the experimental attenuation factor, removing a source of potential error from the calculation.

Several factors were accounted for to obtain the total output energy of the laser. The first factor was the ratio of the active area of the detector to the spot size of both the Daylight Solutions laser and the Rb laser. The calculated energy was divided by the ratio of the Daylight Solutions spot size to detector area (315:1) and multiplied by the same ratio of Rb laser spot area to detector area discussed above (100:1). The value was divided by the percent transmission of the back heat pipe window (~0.86) and broad band pass filter (~0.75) at 2.7 μm . The ratio of percent transmission of the ND filters (<1% difference) and the detector (0.57:0.65) at 2.7 μm and 3.7 μm was also accounted for. The pulse area in Figure 3.4 of 4.5×10^{-9} V•s, which gave $E_{out} = 23.1$ nJ for the blackbody calibration, gave $E_{out} = 35.72$ nJ for the Daylight Solutions calibration. The calibration methods therefore agreed within a factor of 1.5. Because fewer assumptions were required in the Daylight Solutions calibration, this method was used to determine E_{out} for all results that follow.

IR Spot Size and Beam Divergence

To determine the beam shape of the IR laser, the InSb detector was placed on a micrometer and translated across 11 mm at distances of 18 cm and 32 cm from the heat pipe. IR laser energy was plotted as a function of position for both cases. From the full-width at half-maximum (FWHM) of these plots, the divergence of the IR laser was calculated.

In addition, burn patterns of the blue pump pulse from the Continuum ND6000 were recorded (see Figure 4.1). Because the beam quality was poor, determination of the true spot area was difficult. However, an understanding of the spot area was critical, as this was required to estimate the number of Rb atoms in the active volume. Thus, several burn patterns were collected with varying degrees of attenuation (see Figure 4.2).

Laser Excitation Spectra and Measurement of Saturation Broadening

Laser excitation spectra (LES) for both the $5^2S_{1/2} - 6^2P_{1/2}$ and $5^2S_{1/2} - 6^2P_{3/2}$ transitions were obtained by measuring IR laser energy as a function of wavelength across each transition. The dye laser grating was tuned over 0.3 nm in 10 pm step sizes for each transition.

Additionally, the saturation broadening of the spectra was studied. This was done by collecting LES for the $5^2S_{1/2} - 6^2P_{1/2}$ transition with varied degrees of attenuation. Specifically, LES were taken with both an OD-2.0 absorptive ND filter and with no filter in between the dye laser and the heat pipe. By comparing the FWHM of the spectra in both cases, the degree of saturation broadening could be determined.

Rb Laser Output Energy vs. Pump Energy (Energy Scaling)

Energy scaling curves were found for both the $6^2P_{3/2} - 6^2S_{1/2}$ and $6^2P_{1/2} - 6^2S_{1/2}$ laser transitions. This was achieved by measuring the energy per pulse of the IR beam as a function of the energy per pulse of the pump beam at various Rb densities. Temperatures of 190° C, 210° C, 225° C, and 240° C, corresponding with densities of $2.72 \times 10^{14} \text{ cm}^{-3}$, $5.21 \times 10^{14} \text{ cm}^{-3}$, $8.34 \times 10^{14} \text{ cm}^{-3}$, and $1.28 \times 10^{15} \text{ cm}^{-3}$ were used. The dye laser had a maximum energy per pulse in excess of

14.0 mJ, substantially larger than the bleached limit of the IR laser even at the highest attainable Rb density. The pump pulse power was measured by a ThorLabs model D10MM power meter, and converted to energy by dividing by the 10 Hz repetition rate. IR pulse energy was calculated over a range of pump energies from 12.0 mJ/pulse to energies as small as 0.2 mJ/pulse. Because the beam quality was especially poor when operating the dye laser at low power, the experimental setup shown in Figure 3.1 was modified to include a polarizing beam splitting cube and a quarter wave plate. This allowed the pump beam to be sufficiently attenuated to study the power scaling curves near threshold of the IR laser without operating the dye laser at low power.

Rb Laser Output Energy vs. Rb Concentration (Concentration Scaling)

The output energy per pulse of the IR laser was measured as a function of Rb population density in the cell for both the $6^2P_{3/2} - 6^2S_{1/2}$ and $6^2P_{1/2} - 6^2S_{1/2}$ laser transitions. This was achieved by varying the temperature of the cell while holding the pump energy constant. The temperature was varied from 80° C to 210° C in 10° C increments, corresponding with Rb densities of $1.1 \times 10^{12} \text{ cm}^{-3}$ to $1.4 \times 10^{15} \text{ cm}^{-3}$. The pump energy used for this experiment was 10.0 mJ/pulse, well beyond the maximum observed E_{pump} required to bleach the cell ($<2 \text{ mJ}$).

Pulsed Absorption Spectra

One of the major goals of this work was to demonstrate that the mid-IR Rb laser was significantly more efficient than demonstrated by Richards. The hypothesis for the low efficiency demonstrated by Richards was that the number of pump photons available far exceeded the number of Rb atoms in the active volume of the heat pipe. That is, the pump energy was orders of

magnitude larger than required to bleach the cell. This could be shown if the absorbance of both pump transitions was small, even at very small pump energies.

To demonstrate this, an absorption spectrum was collected using the setup in Figure 3.7.

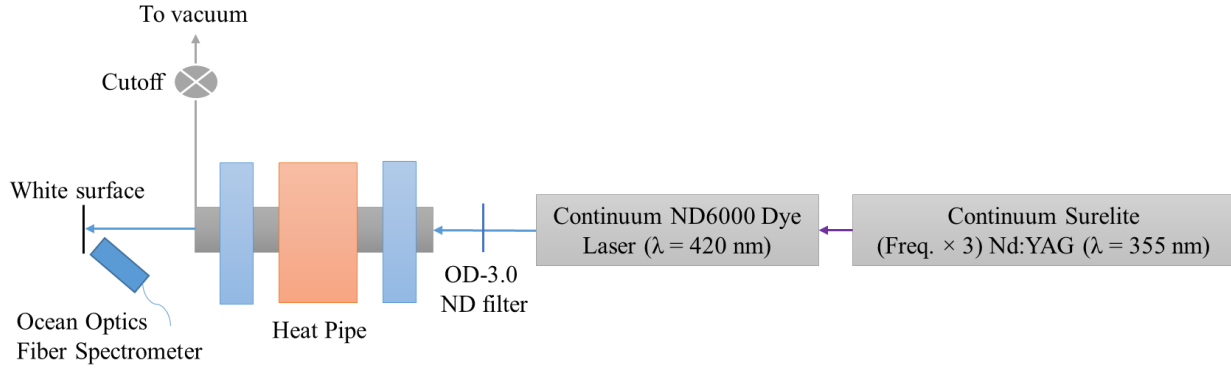


Figure 3.7. Pulsed-pump absorption spectroscopy setup.

To show that the percentage of the on-resonance pump beam was low even at low pump energies, a ThorLabs absorptive OD-3.0 ND filter was placed between the dye laser and the heat pipe. This attenuated the 10 mJ pump beam by a factor of 10^3 . The pump beam was then passed through the heat pipe. The portion of the blue beam that was not absorbed by the vaporous Rb atoms in the cell was incident on a white surface. An Ocean Optics fiber spectrometer (model number QP400-2-VIS-NIR) measured the intensity of the blue light reflected off the white surface when the dye laser was both on and off resonance. The dye laser was tuned over a range of 4 nm at a rate of 1 pm/sec. The measured intensity in arbitrary units (AU) was plotted as a function of wavelength. Absorbance for both the $5^2S_{1/2} - 6^2P_{1/2}$ and $5^2S_{1/2} - 6^2P_{3/2}$ pump transitions was calculated from the ratio of the on-resonance and off-resonance intensities.

Continuous Wave (cw) Diode Pump Experiments

All of the pulsed laser experiments described above used the setup shown in Figure 3.1. Additional experiments were conducted using a cw blue diode laser as the pump source. These included the collection of absorption spectra for both pump transitions at various Rb number densities, as well as an unsuccessful attempt to demonstrate a cw mid-IR Rb laser.

The laser used was a Topicta Photonics BlueTune diode laser. The BlueTune laser had a central wavelength of 420.2 nm with a 1 GHz bandwidth and a 23 GHz tuning range. Pump laser wavelength varied with current, from the threshold value of 25 mA to a maximum of 55 mA. The maximum output power was 38.9 mW, with a spot area of 3.1 mm². The setup for the cw experiments is shown in Figures 3.8 (absorption spectra) and 3.9 (cw mid-IR Rb laser).

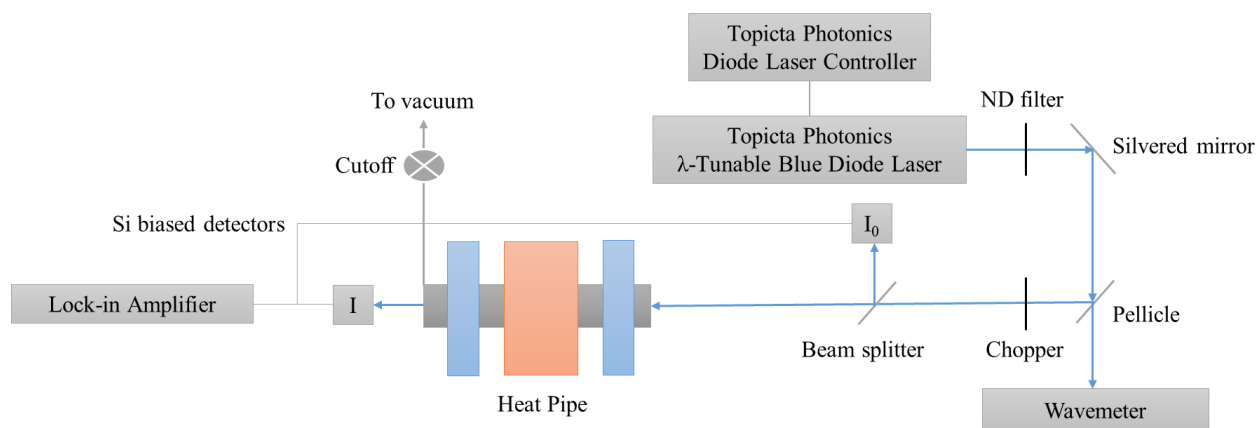


Figure 3.8. Setup for cw absorption spectroscopy experiments.

Figure 3.8 shows the experimental setup for the laser absorption spectroscopy experiments performed with the BlueTune tunable diode laser. The beam was attenuated by an OD-1.0 ND filter, so that the photodiodes were not overfilled, and then split by a pellicle, sending a portion to a wavelength meter to measure the frequency of the diode laser as it was tuned. The beam was

then split again by a 50/50 (non-polarized) beam splitting cube, sending half the light to the first photodiode (I_0) and the other half through the cell and to the second photodiode (I). Both photodiodes were connected to a lock-in amplifier. The ratio of I/I_0 was measured across the tuning range of diode laser to find the absorption of the cell as a function of wavelength. Absorption spectra were found for both the 421.7 nm $5^2S_{1/2} - 6^2P_{1/2}$ and 420.2 nm $5^2S_{1/2} - 6^2P_{3/2}$ transitions at Rb concentrations of 1.07×10^{12} , 4.64×10^{12} , 1.43×10^{13} , 3.76×10^{13} , 8.47×10^{13} , 1.88×10^{14} , and $3.25 \times 10^{14} \text{ cm}^{-3}$.

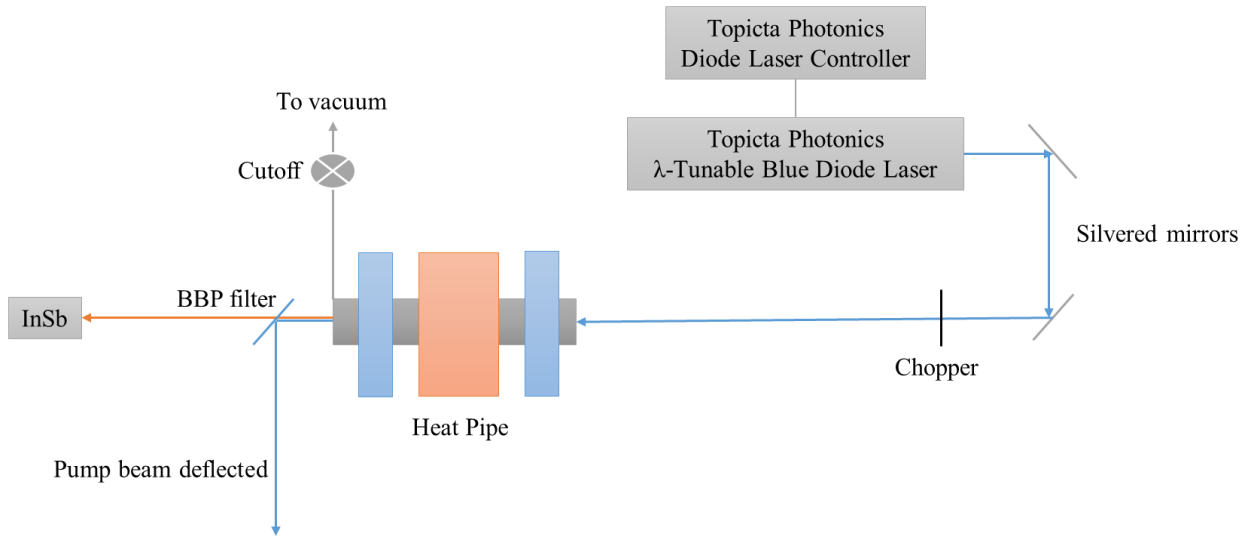


Figure 3.9. Setup for attempted cw IR laser demonstration

Additionally, an attempt was made to demonstrate a cw mid-IR Rb laser to recreate and better understand the work of Sharma. This was done using the setup shown in Figure 3.9. The BlueTune diode laser was used as the pump source. The beam was passed through the heat pipe, and the pump beam was deflected by a ThorLabs 2.75 μm broad band pass filter. The same Teledyne Judson InSb detector was used to look for the IR laser, but no IR signal was found. The possible reasons for this are discussed in Chapter IV.

IV. Results

Chapter Overview

In this chapter, the results of the experiments conducted to characterize the mid-IR Rb laser are discussed in detail. In addition, potential sources of error and uncertainty are outlined.

Beam Shape

The burn pattern of the pump beam on Kentek burn paper (model Z-24) is shown in Figure 4.1. As is typical with high-power pulsed lasers, the beam quality was poor. The beam spot had an irregular, crescent-like shape, likely due to alignment of optics within the dye laser.



Figure 4.1. Pump beam shape. The diameter of the laser spot was approximately 5 mm, but was concentrated into a crescent shape.

In order to determine the active volume of the heat pipe, and thus the number of Rb atoms in the path of the pump laser, the true area of the pump laser had to be well known. To get a better estimate of the spot size, burn patterns were collected using increasing levels of attenuation. These burn patterns are shown in Figure 4.2.



Figure 4.2. Pump beam shape with increasing attenuation. From left to right: unattenuated, attenuated with an OD-0.1 ND filter, attenuated with an OD-0.2 ND filter, attenuated with an OD-0.3 ND filter. The area of the unattenuated spot was 7.10 mm^2 , and the area of the most highly attenuated spot was approximately 10 percent of this value. No beam pattern was visible on the burn paper for attenuation with an OD-0.4 ND filter or greater.

According to Richards, the unattenuated beam spot had an area of 7.10 mm^2 (Richards, 2013:38). However, increasing levels of attenuation revealed that the pump photons were concentrated into a small sliver. Using pixel threshold analysis, the beam area of the most highly attenuated spot was found to be 14 percent that of the unattenuated spot. This gave an estimated spot area of $\sim 1 \text{ mm}^2$. Using this spot area and the estimated gain path length of 10.2 cm, at 220°C , or a number density of $1.96 \times 10^{15} \text{ cm}^{-3}$, there were approximately 2×10^{14} atoms in the active volume. See the section later in this chapter on Output Energy vs. Rb Concentration for further discussion on the impact of spot size and active volume on scaling the laser.

The shape of the IR beam was analyzed by placing the detector on a micrometer some distance z from the exit window of the heat pipe and scanning in the x (horizontal) direction across the profile of the beam. A graph of IR laser energy vs. x position of the detector for both $z = 18 \text{ cm}$ and $z = 32 \text{ cm}$ is shown in Figure 4.3.

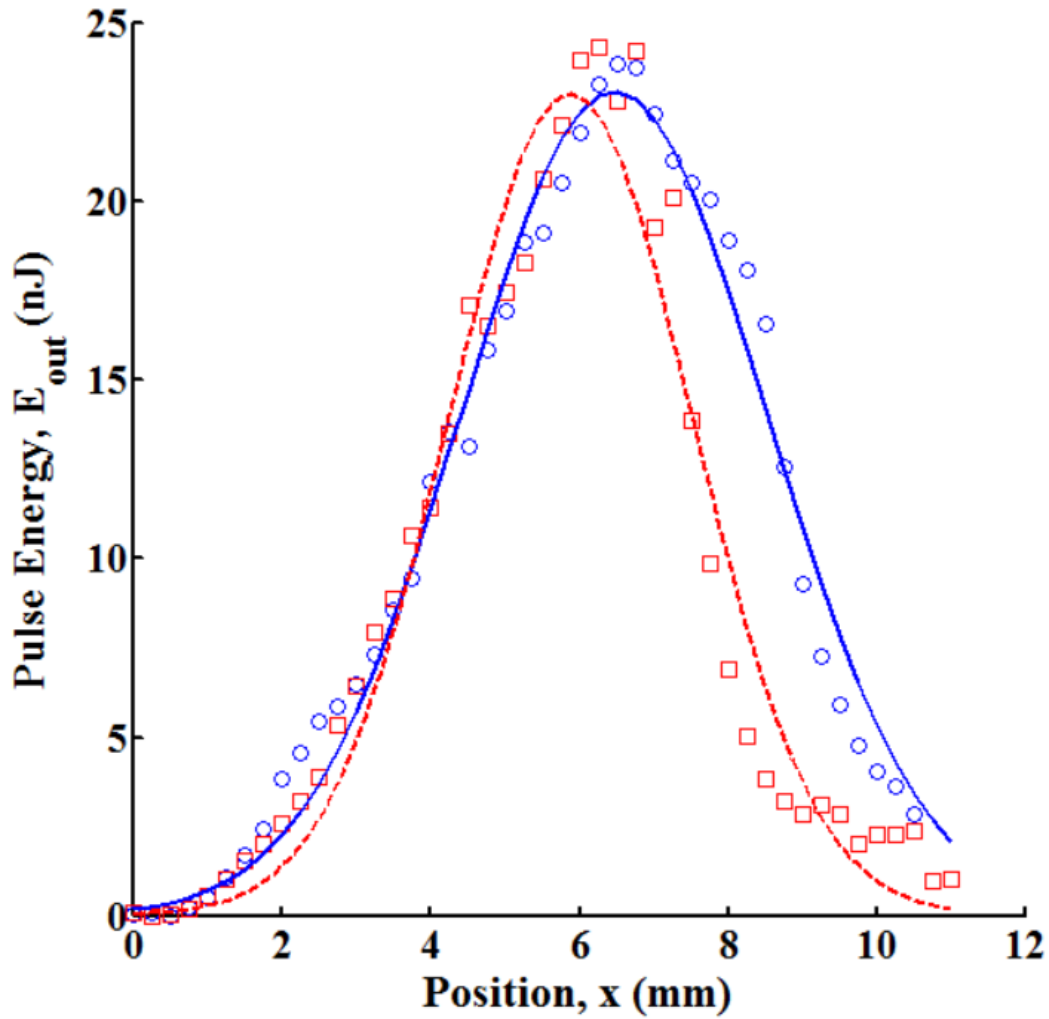


Figure 4.3. IR beam shape at two different distances (z) from the heat pipe exit to the detector. The data shown in red (\square) was taken at $z = 18$ cm; the data in blue (\circ) was taken at $z = 32$ cm. Because of the poor beam quality of the pump beam shown in Figure 4.1 and 4.2, the shape of these spatial profiles is asymmetrical and therefore poorly fit by a Gaussian curve. For this reason, the Gaussian fit was used solely as an estimate of the FWHM of the spatial profiles. The FWHM was 3.46 mm at $z = 18$ cm and 4.62 mm at $z = 32$ cm.

The data were fit to Gaussian curves using Equation 4.1:

$$E_{out} = A e^{-[(x-B)/C]^2}, \quad (1)$$

where the fit parameters A, B, and C for both distances are given in Table 4.1. It can be seen from Figure 4.3 that the spatial scan data are poorly fit by Gaussian curves. The asymmetry of the data

was due to the poor beam quality of the pump laser seen in Figures 4.1 and 4.2. The Gaussian fits were therefore used only to get an estimate of the FWHM of the IR laser spot. This could be used to estimate the divergence of the IR laser.

Table 4.1: IR Beam Shape Fit Parameters

z (cm)	A (nJ)	B (mm)	C (mm)
18	23.03	5.878	2.32
32	23.1	6.459	2.921

The beam divergence, θ , was found using Equation 4.2:

$$\theta = \frac{FWHM_2 - FWHM_1}{z_2 - z_1}, \quad (2)$$

where the FWHM of the Gaussian curve is found from the MATLAB curve-fitting tool and z is the distance from the heat pipe exit. The divergence of the IR laser was calculated to be 6.44 mrad.

Because the heat pipe was not part of a laser cavity but was instead used as a single-pass gain cell, the divergence in the x-direction should be approximately equal to the beam width in the x-direction divided by the gain path length, $\theta = d/l_g$. If the photons are assumed to be concentrated into the sliver shown in the OD-0.3 attenuated burn pattern in Figure 4.2, the thickness in the x-direction of the pump beam spot through the cell, d , is $\sim 0.75 \pm 0.5$ mm. As discussed in Chapter III, the path length l_g , had a range of possible values from 10.2 cm to 17.5 cm. Thus, if the spot thickness were taken to be 1.25 mm, the divergence θ would range from 7.35 mrad at $l_g = 10.2$ cm to 4.29 mrad at $l_g = 17.5$ cm, in good agreement with the result calculated using Figure 4.3 and Equation 4.2. The experimental divergence of 6.44 mrad would correspond with a value of $l_g \sim 13$ cm if $d = 0.75$ mm.

These results could be used to estimate the spot size of the IR beam at the detector. As discussed in Chapter III, the IR spot size was important to know because the spot area was significantly larger than the detector area (0.01 mm²). The total output energy of the IR laser could be found from the product of the energy received by the detector and the ratio of the spot area to the detector area. As mentioned above, the heat pipe was used as a single-pass gain cell, so the area of the IR spot at the detector could be estimated geometrically using Equation 4.3

$$A = \left(\frac{z}{l_g} \right)^2 A_0, \quad (3)$$

where A_0 is the area of pump beam (~ 1 mm²), z is the distance from the rear edge of the gain path length to the detector and l_g is the gain path length. The InSb was 18 cm from the rear window of the heat pipe for all experiments. In Equation 4.3, z is the distance from the edge of the gain path length, not from the rear window of the detector. Thus, z was dependent on the path length, with a minimum of ~ 27 cm if $l_g = 17.5$ cm and a maximum of ~ 31 cm if $l_g = 10.2$ cm. This gave a range of possible IR spot areas at the detector from 2.35 mm² to 8.66 mm².

As discussed, E_{out} was found from the ratio of the IR spot area and detector area. The minimum value of 2.35 mm² was chosen for the calibration in all results that follow. As E_{out} increases with A , the most conservative estimate was chosen so that the maximum reported E_{out} would not be overstated.

Laser Excitation Spectra

Figure 4.4 shows the spectral features of the $5^2S_{1/2} - 6^2P_{3/2}$ and $5^2S_{1/2} - 6^2P_{1/2}$ transitions. Gaussian curves were fit to the data using Equation 4.4:

$$E_{out} = A e^{-[(\lambda-B)/C]^2}, \quad (4)$$

where the fit parameters A, B, and C for both distances are given in Table 4.2. The FWHM of the $5^2S_{1/2} - 6^2P_{3/2}$ (420.2 nm) peak was 0.104 nm, or 176.7 GHz, and the FWHM of the $5^2S_{1/2} - 6^2P_{1/2}$ (421.7 nm) peak was 0.089 nm, or 150.1 GHz.

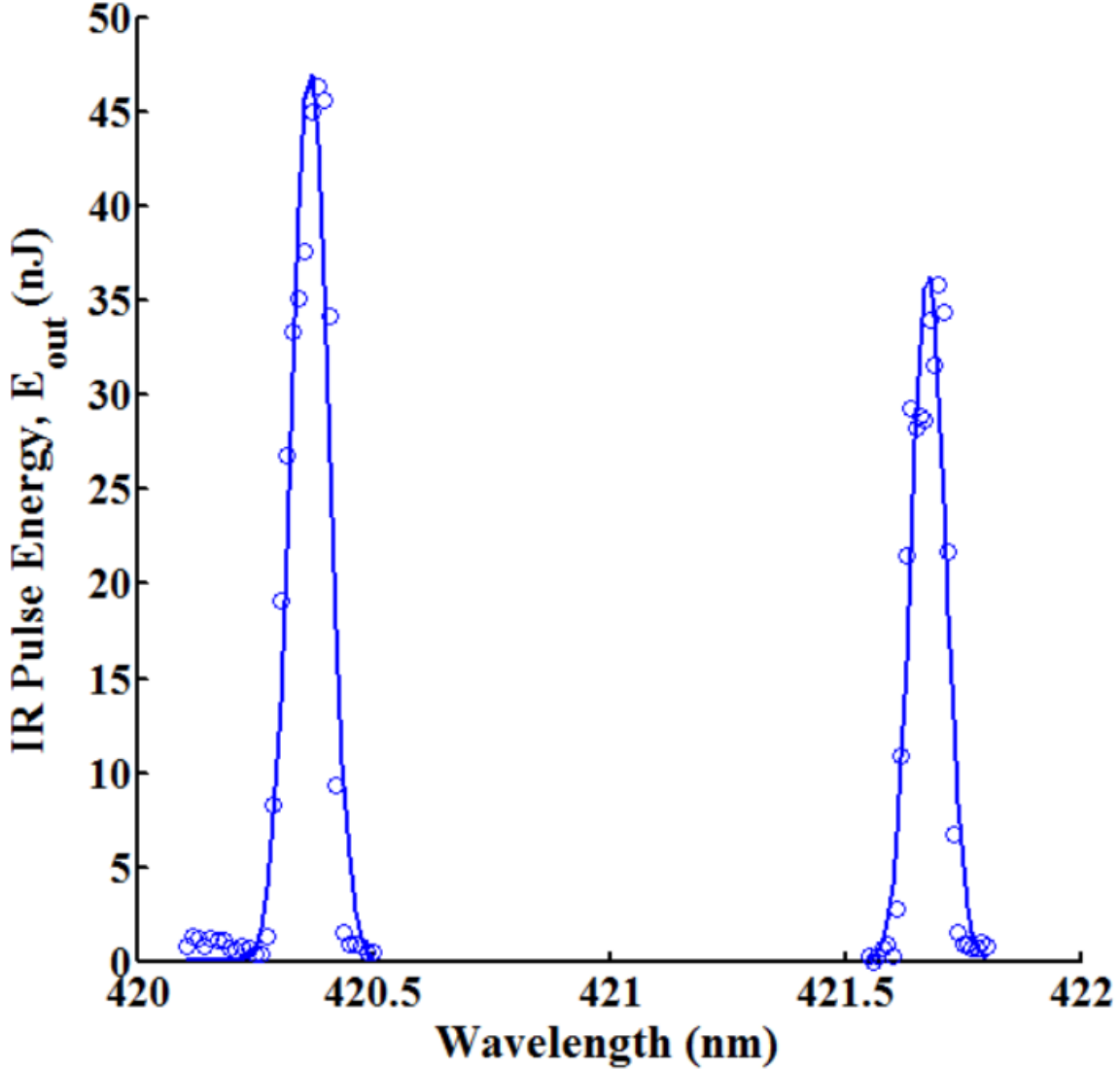


Figure 4.4. Laser excitation spectra of both the $5^2S_{1/2} - 6^2P_{3/2}$ and $5^2S_{1/2} - 6^2P_{1/2}$ transitions. Asymmetries in both peaks are due to hyperfine structure. The hyperfine structure is more clearly resolved in the cw absorption experiments (see Figures 4.15 and 4.16).

Table 4.2: Laser Excitation Spectra Fit Parameters

Transition Wavelength	A (nJ)	B (nm)	C (nm)
420.2 nm	47.21	420.3	0.05705
421.7 nm	36.38	421.7	0.05719

Several useful pieces of information can be extracted from this data. The first and most obvious is the clear indication that the IR laser was indeed produced. Only when the dye laser was on-resonance for the two pump transitions did the InSb receive an infrared signal. At all other wavelengths, the IR signal received by the detector was approximately zero. Also, the data indicate that the $5^2S_{1/2} - 6^2P_{3/2}$ (420.2 nm) transition has a higher efficiency than the $5^2S_{1/2} - 6^2P_{1/2}$ transition, which is supported by the scaling data presented in Figures 4.6, 4.7, and 4.12.

Some asymmetries appear in Figure 4.4 in both transitions. These were due to hyperfine structure. It was not possible to fully resolve the hyperfine structure for the pulsed laser excitation spectra, as the 10 pm step size was too large. However, the hyperfine structure was very clearly resolved in the cw absorption spectroscopy experiments (see Figures 4.15 and 4.16).

Additionally, it is apparent that the spectral lines are very broad compared to the Doppler width, calculated using Equation 2.3. As mentioned above, at 160° C, the temperature of the heat pipe when the data from Figure 4.4 was taken, the Doppler widths of the pump transitions were 1.14 GHz ($5^2S_{1/2} - 6^2P_{1/2}$) and 1.15 GHz ($5^2S_{1/2} - 6^2P_{3/2}$). As the heat pipe was in vacuum, this significant broadening was not caused by collisional processes. Instead, the spectral lines were saturation broadened due to the very large pump energy. Figure 4.5 shows the effect of saturation broadening at multiple pump energies on the $5^2S_{1/2} - 6^2P_{1/2}$ spectral peak. The Gaussian curves were fit using Equation 4.5. The fit parameters A, B, and C are given in Table 4.3.

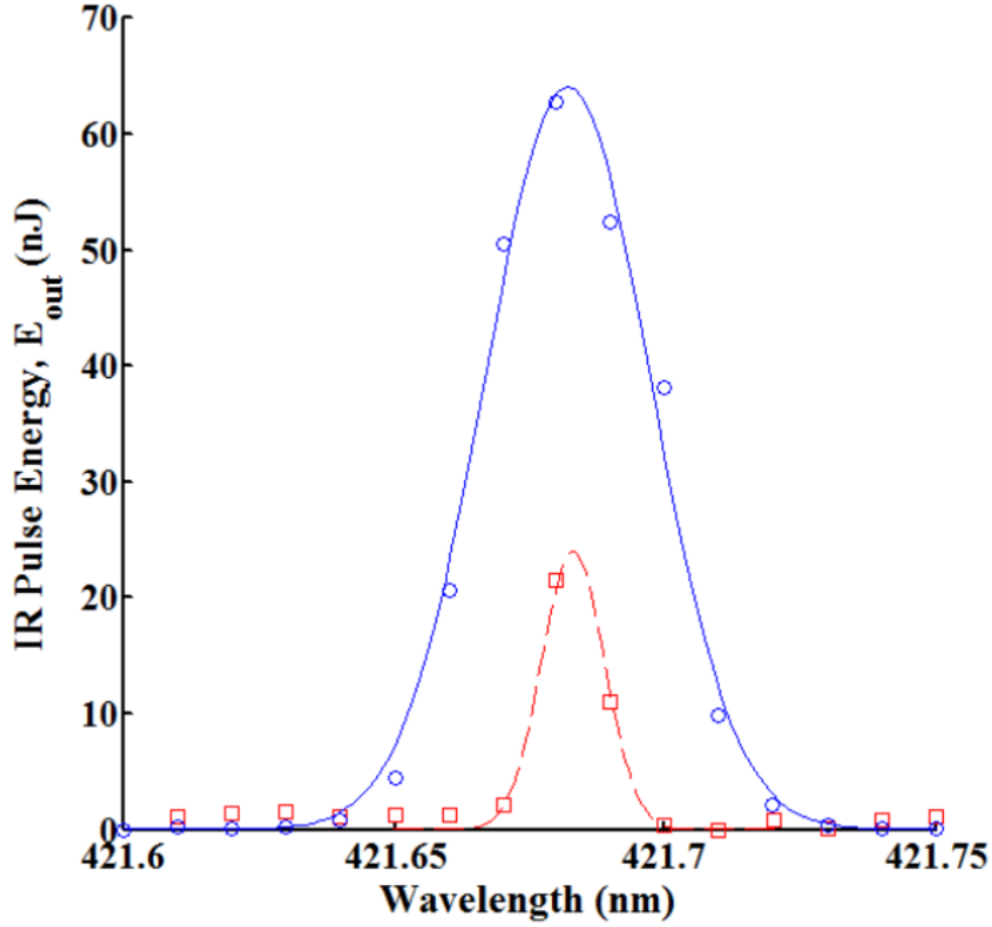


Figure 4.5: Effect of saturation broadening. Spectra of the $5^2S_{1/2}$ - $6^2P_{1/2}$ transition are shown at pump energies of 0.05 mJ (\circ) and 1.0 mJ (\square). The FWHM of the spectral feature broadens from 16.01 pm to 36.32 pm, a factor of 2.27, as $\sqrt{I/I_{sat}}$ increases by a factor of about 4.5.

Table 4.3: Saturation Broadening Fit Parameters

Pump Energy (mJ)	A (nJ)	B (nm)	C (nm)
0.05	24.07	421.683	0.008187
1.00	64.12	421.682	0.02168

From Figure 4.5, it can be seen that the FWHM of the entire feature increases significantly as the pump energy is increased. The degree of saturation broadening can be calculated theoretically using Equation 4.5 (Demtröder, 1982):

$$\Delta\nu_{sat} = \sqrt{1 + \frac{I}{I_{sat}}} \Delta\nu_D, \quad (5)$$

where $\Delta\nu_D$ is the Doppler linewidth, I is the intensity of the pump beam, and the saturation intensity, I_{sat} , was calculated using Equation 4.6:

$$I_{sat} = \frac{h\nu_{kj}(A_{kj} + A_{ik})}{\sigma_{kj}}, \quad (6)$$

where h is the Planck constant, A_{kj} is the Einstein A coefficient of the laser transition, A_{ik} is the Einstein A coefficient of the pump transition, and σ_{kj} is the cross section of the laser transition. It should be noted that Equation 4.5 is intended for homogeneous broadening. However, in this case the laser bandwidth of ~ 2 GHz was on the order of the Doppler width. Thus, the width of the hole burned was approximately the transition width, and Equation 4.5 could be used (Demtröder, 1982).

For the 421.7 nm transition, the saturation intensity is 351.4 mW/m². As mentioned above, it was difficult to exactly determine the area of the spot size, and thus the intensity of the pump beam. However, taking the spot area to be an approximate value of 4.91 mm², the intensity of the laser at a pump energy of 0.05 mJ was 10.2 mW/cm². Thus $I/I_{sat} \sim 290$, so $\Delta\nu_{sat}$ should have been about 17 times larger than the Doppler width. This agrees well with experimental result that $\Delta\nu_{sat}$ was 15 times larger than the Doppler width. For the 1.0 mJ pump, $I/I_{sat} \sim 5796$, so $\Delta\nu_{sat}$ should have been about $76\Delta\nu_D$, in reasonable agreement with the experimental result of $53\Delta\nu_D$.

Rb Laser Output Energy vs. Pump Energy

Plots of IR energy per pulse as a function of pump energy per pulse are shown in Figures 4.6 and 4.7 for the $6^2P_{3/2} - 6^2S_{1/2}$ (2.73 μm) and $6^2P_{1/2} - 6^2S_{1/2}$ (2.79 μm) transitions, respectively,

at four different Rb concentrations, ranging from $2.72 \times 10^{14} \text{ cm}^{-3}$ to $1.28 \times 10^{15} \text{ cm}^{-3}$. The data were fit according to Equation 4.7,

$$E_{out} = E_{bl} [1 - e^{-\eta(E_{pump} - E_{th})/E_{bl}}], \quad (7)$$

where the E_{out} is the laser output energy, E_{bl} is the maximum output energy (bleached limit), η is the slope efficiency, E_{pump} is the pump energy, and E_{th} is the threshold pump energy. The fit parameters for both transitions are provided in Table 4.4.

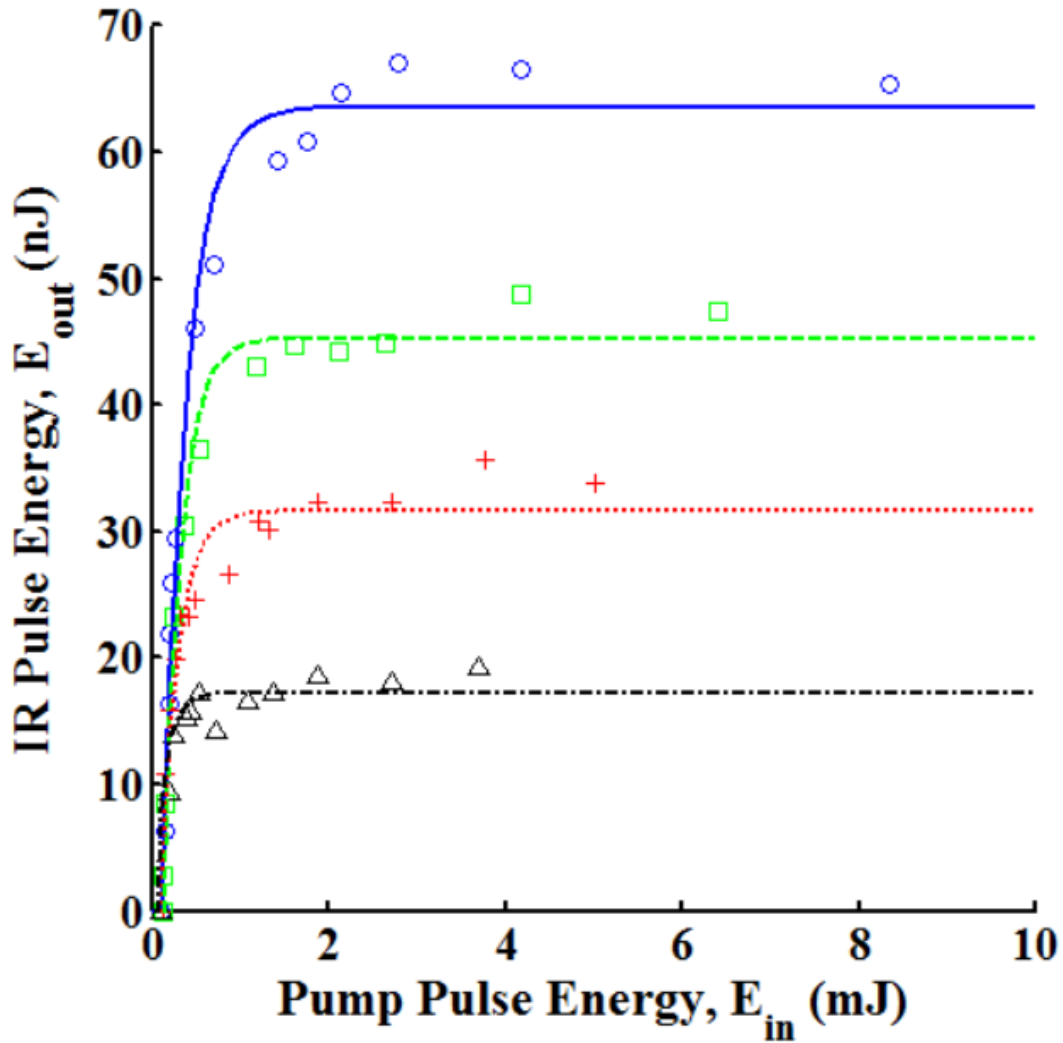


Figure 4.6. Output IR energy per pulse as a function of pump pulse energy for the $6^2P_{3/2} - 6^2S_{1/2}$ ($2.73 \text{ }\mu\text{m}$) transition at four different Rb densities: $2.72 \times 10^{14} \text{ cm}^{-3}$ (Δ), $5.21 \times 10^{14} \text{ cm}^{-3}$ (+), $8.34 \times 10^{14} \text{ cm}^{-3}$ (\square), and $1.28 \times 10^{15} \text{ cm}^{-3}$ (\circ).

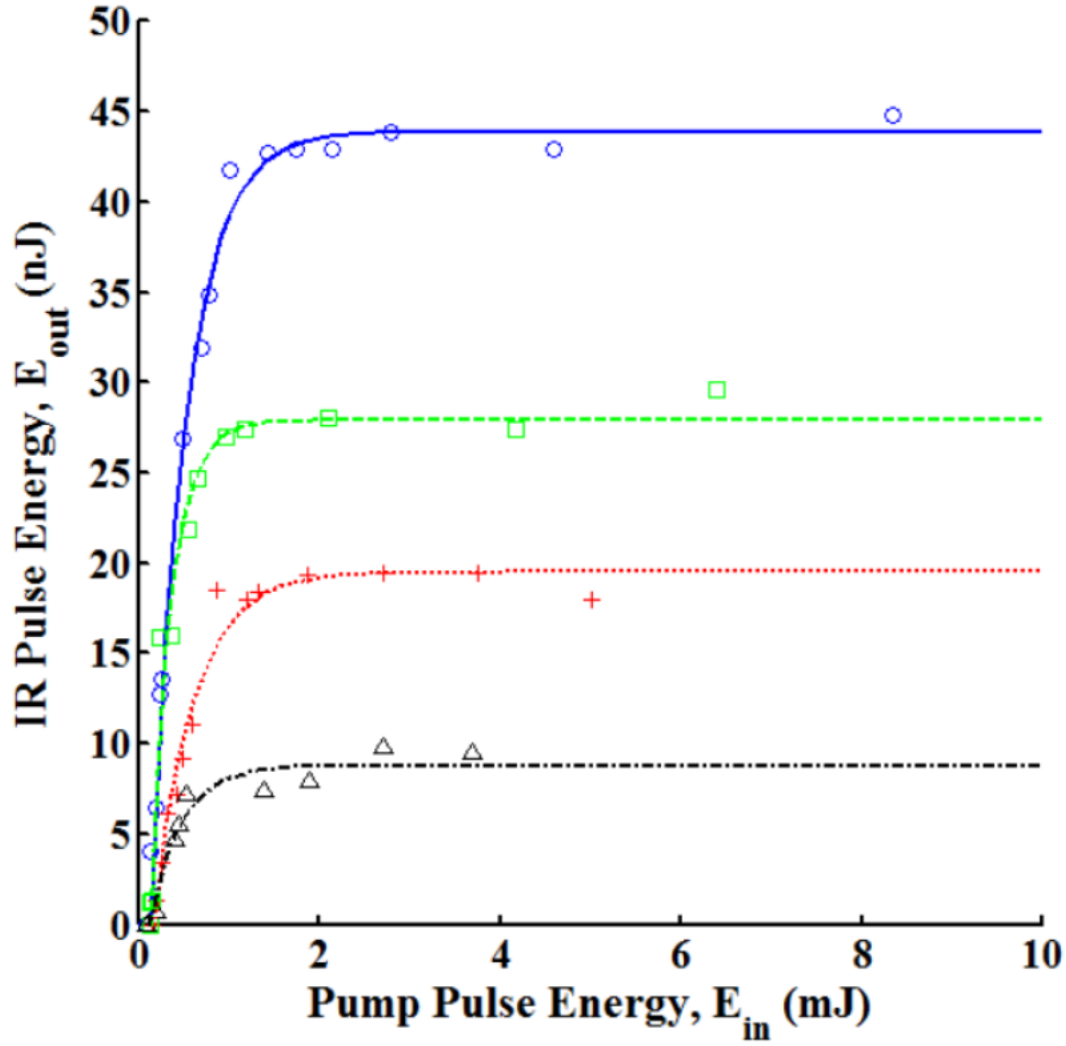


Figure 4.7. Output IR energy per pulse as a function of pump pulse energy for the $6^2P_{1/2} - 6^2S_{1/2}$ ($2.79 \mu\text{m}$) transition at four different Rb densities: $2.72 \times 10^{14} \text{ cm}^{-3}$ (Δ), $5.21 \times 10^{14} \text{ cm}^{-3}$ (+), $8.34 \times 10^{14} \text{ cm}^{-3}$ (\square), and $1.28 \times 10^{15} \text{ cm}^{-3}$ (\circ).

Table 4.4. Energy Scaling Fit Parameters

Rb Density (10^{14} cm^{-3})	Bleached Limit, E_{bl} (nJ)		Threshold Energy, E_{th} (μJ)		Slope Efficiency, η ($\times 10^{-4}$)	
	$6^2P_{3/2} - 6^2S_{1/2}$	$6^2P_{1/2} - 6^2S_{1/2}$	$6^2P_{3/2} - 6^2S_{1/2}$	$6^2P_{1/2} - 6^2S_{1/2}$	$6^2P_{3/2} - 6^2S_{1/2}$	$6^2P_{1/2} - 6^2S_{1/2}$
12.8	63.57 ± 1.4	43.9 ± 1.1	104 ± 12	124 ± 10	2.36 ± 0.29	1.12 ± 0.12
8.34	45.3 ± 0.9	27.9 ± 0.1	112 ± 7	116 ± 10	2.21 ± 0.24	1.19 ± 0.19
5.21	31.6 ± 1.1	19.5 ± 0.6	82 ± 20	160 ± 20	1.61 ± 0.31	0.44 ± 0.05
2.72	17.2 ± 0.57	8.8 ± 0.5	92 ± 10	115 ± 30	1.53 ± 0.28	0.25 ± 0.05

The plots of input energy vs. output energy from Richards' experiment are shown in Figures 4.8 and 4.9 (Richards, 2013:24-25).

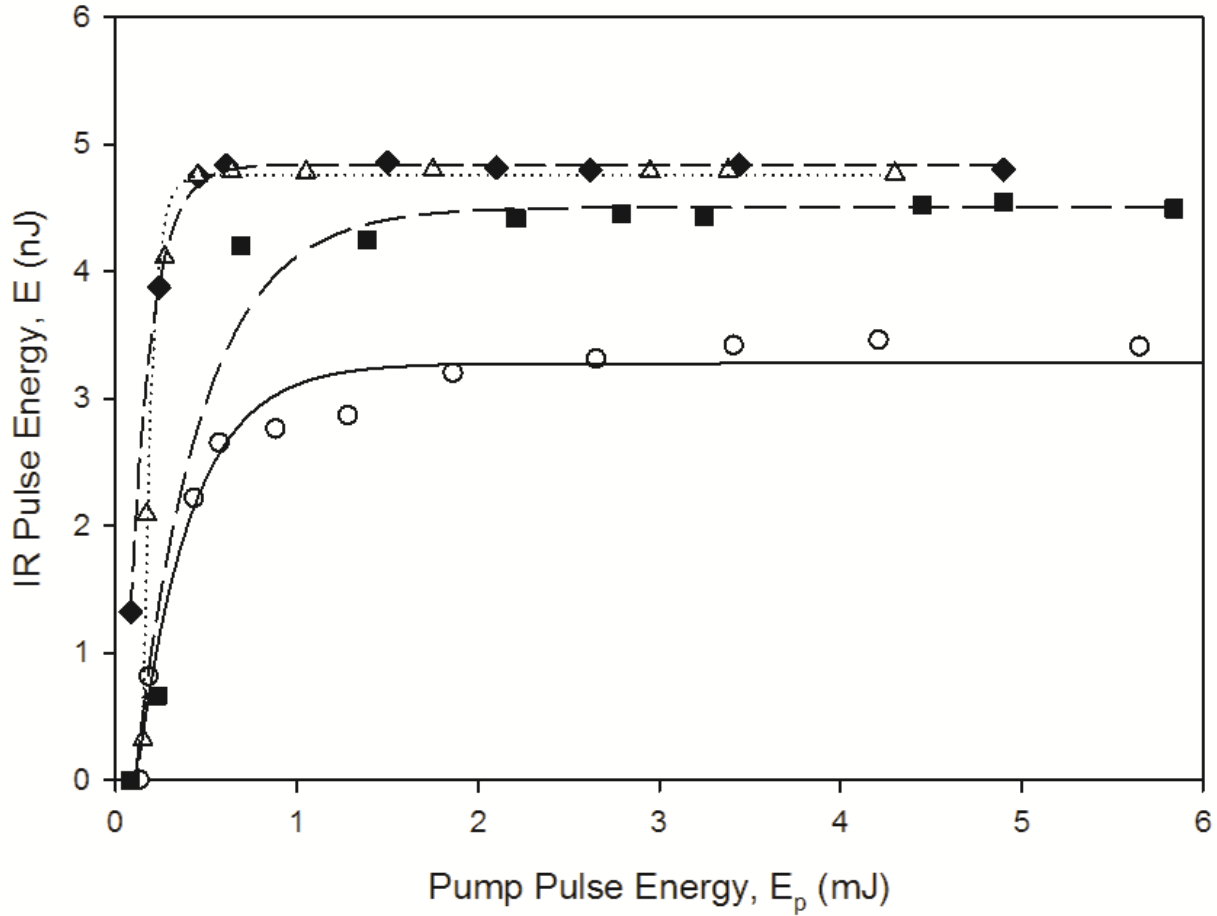


Figure 4.8. Richards' data for Output IR energy per pulse as a function of pump pulse energy for the $6^2P_{3/2} - 6^2S_{1/2}$ ($2.73 \mu\text{m}$) transition at four different Rb densities: $6.5 \times 10^{13} \text{ cm}^{-3}$ (o), $1.4 \times 10^{14} \text{ cm}^{-3}$ (■), $2.8 \times 10^{14} \text{ cm}^{-3}$ (Δ), and $5.2 \times 10^{14} \text{ cm}^{-3}$ (◆) (Richards, 2013:24).

Several key differences can be seen immediately. A significant trend that appears in Richards' data was not observed in this experiment. Richards reported that the bleached limit of the IR laser did not increase with additional Rb density beyond $n \sim 2.5 \times 10^{14} \text{ cm}^{-3}$. In fact, for the $6^2P_{1/2} - 6^2S_{1/2}$ laser, Richards reported a decrease in bleached limit as Rb density rose from $2.8 \times 10^{14} \text{ cm}^{-3}$ to $5.2 \times 10^{14} \text{ cm}^{-3}$.

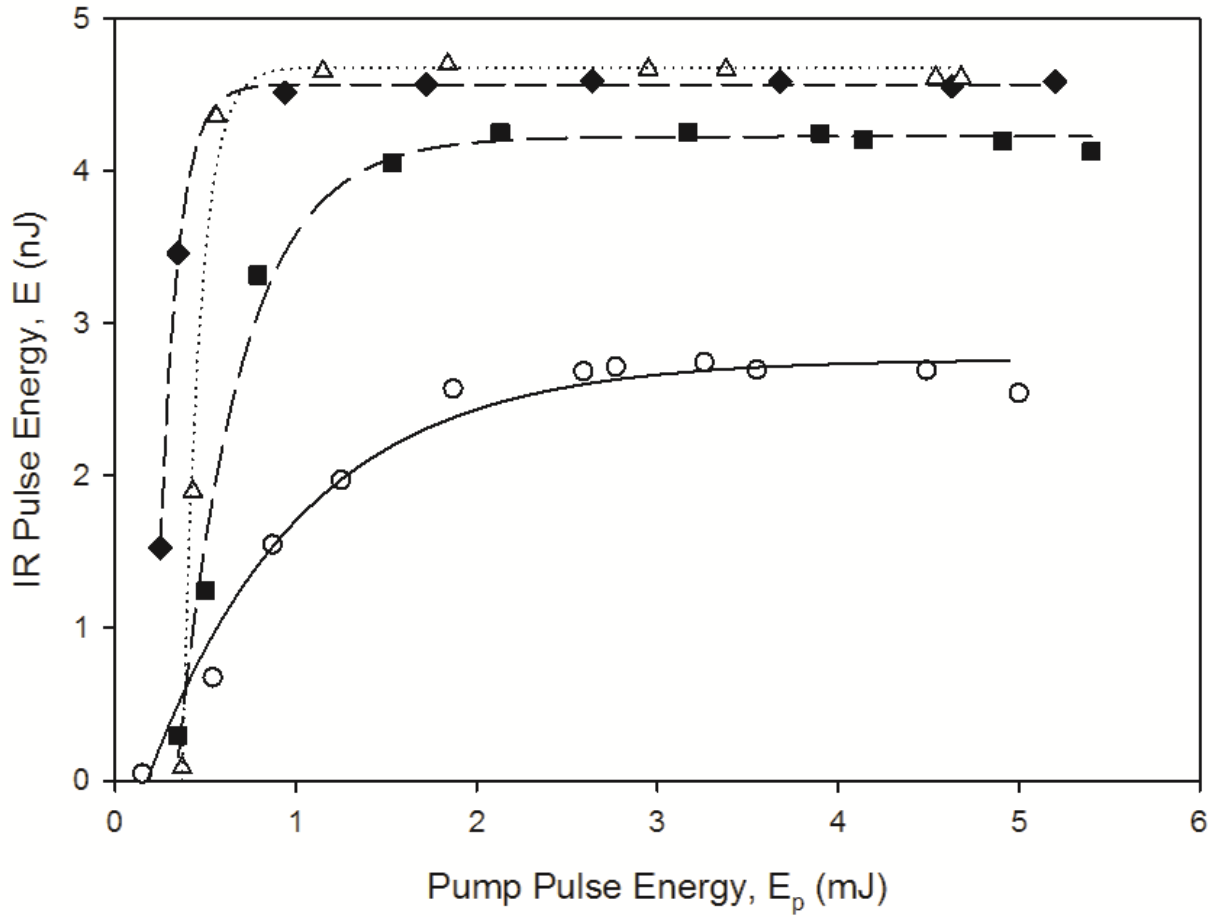


Figure 4.9. Richards' data for Output IR energy per pulse as a function of pump pulse energy for the $6^2P_{1/2} - 6^2S_{1/2}$ ($2.79 \mu\text{m}$) transition at four different Rb densities: $6.5 \times 10^{13} \text{ cm}^{-3}$ (o), $1.4 \times 10^{14} \text{ cm}^{-3}$ (■), $2.8 \times 10^{14} \text{ cm}^{-3}$ (Δ), and $5.2 \times 10^{14} \text{ cm}^{-3}$ (◆) (Richards, 2013:25).

The data presented in Figures 4.6 and 4.7 clearly show this trend to be false. Bleached limit increases linearly with added Rb concentration. There is no indication of the rollover observed by Richards, even at Rb densities an order of magnitude larger than Richard's supposed rollover point. A plot of the bleached limit of the IR laser as a function of Rb concentration is shown in Figure 4.10. For Richards' corresponding figure, see the Appendix.

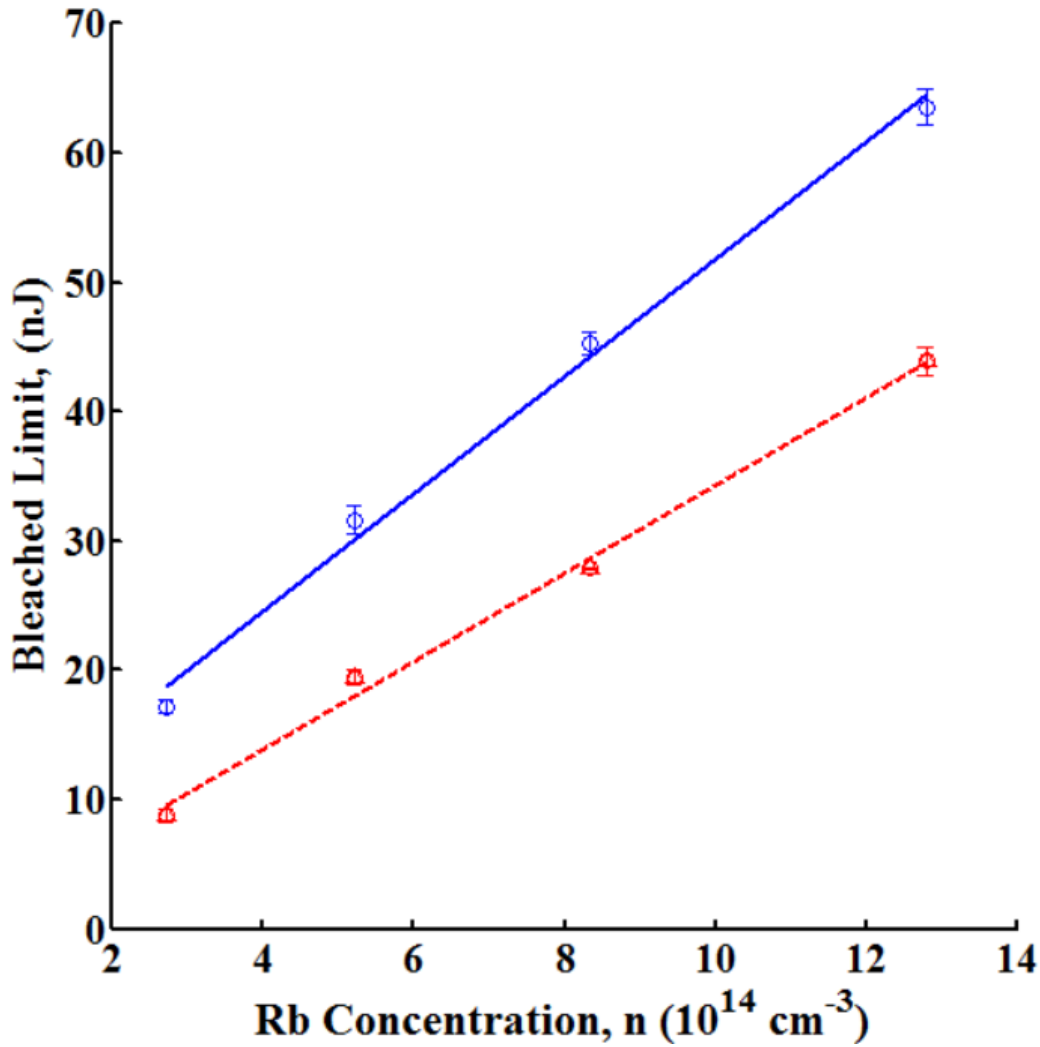


Figure 4.10. Bleached limit as a function of Rb concentration for the $6^2P_{1/2} - 6^2S_{1/2}$ (Δ) and $6^2P_{3/2} - 6^2S_{1/2}$ (\circ) transitions. Bleached limit scales linearly with increasing Rb density for both transitions, even at Rb concentrations above $n = 10^{15} \text{ cm}^{-3}$. This contradicts Richards' data, which suggests bleached limit levels off at an Rb concentration of $\sim 2.5 \times 10^{14} \text{ cm}^{-3}$.

A plot of slope efficiency as a function of Rb concentration is shown in Figure 4.11. In this figure and the corresponding figure from Richards (see the Appendix), slope efficiency increased roughly linearly with increasing Rb concentration. Figure 4.11 shows a maximum observed slope efficiency of 2.3×10^{-4} , an improvement from Richards by about an order of magnitude.

Slope efficiency was a difficult parameter to measure accurately because of several factors. Primarily, bleaching occurred very quickly (<1 mJ), leading to a small number of possible data points in the region of linear growth in Figures 4.6 and 4.7. Furthermore, the Coherent FieldMax II power meter (model D10MM) used to measure the pump energy, which was the same for both this experiment and Richards', had a noise threshold of about 0.5 mJ. Given the fact that bleaching occurred before E_{pump} reached 1 mJ, uncertainty in the measurements of E_{pump} , especially very close to threshold, led to large uncertainty in the calculation of slope efficiency. This is reflected in the large error bounds shown in Figure 4.11.

However, threshold could be estimated for this laser theoretically. Since there is no spin-orbit process before lasing can occur as in the traditional DPAL, threshold should occur at an inversion that can be found from Equation 4.8,

$$\sigma l \Delta N \approx 20, \quad (8)$$

where σ is the cross section, l is the gain path length, and ΔN is the population inversion (Verdeyen, 1989). Given the stimulated emission cross section of the $5^2S_{1/2} - 6^2P_{3/2}$ transition of $9.83 \times 10^{-11} \text{ cm}^2$ and the estimated gain path length of 17.5 cm, the population inversion required to reach threshold was approximately $1.16 \times 10^{10} \text{ cm}^{-3}$. This inversion was achieved at a heat pipe temperature of 26.5° C, which agrees with Sharma's observation that threshold is approximately instantaneous (Sharma, 1981:210).

Given this information, it can be inferred that slope efficiency did indeed grow linearly with increased Rb concentration, despite the possible interpretation of the data from Figure 4.11 that slope efficiency rolls over between $8.34 \times 10^{14} \text{ cm}^{-3}$ and $1.28 \times 10^{15} \text{ cm}^{-3}$. If threshold is approximately zero, the slope efficiency should continue to grow linearly as a function of Rb concentration as long as the bleached limit does as well. This is demonstrated in Figure 4.10, it is

highly likely that slope efficiency should continue to rise with increased Rb density. This could be seen more clearly by either measuring the pump energy with a detector with a lower noise threshold, or by examining E_{in} vs E_{out} at a Rb concentration in the heat pipe such that the number of excitable Rb atoms more closely matches the number of pump photons. In this case, bleaching would occur much less quickly, and the slope efficiency could be more easily measured.

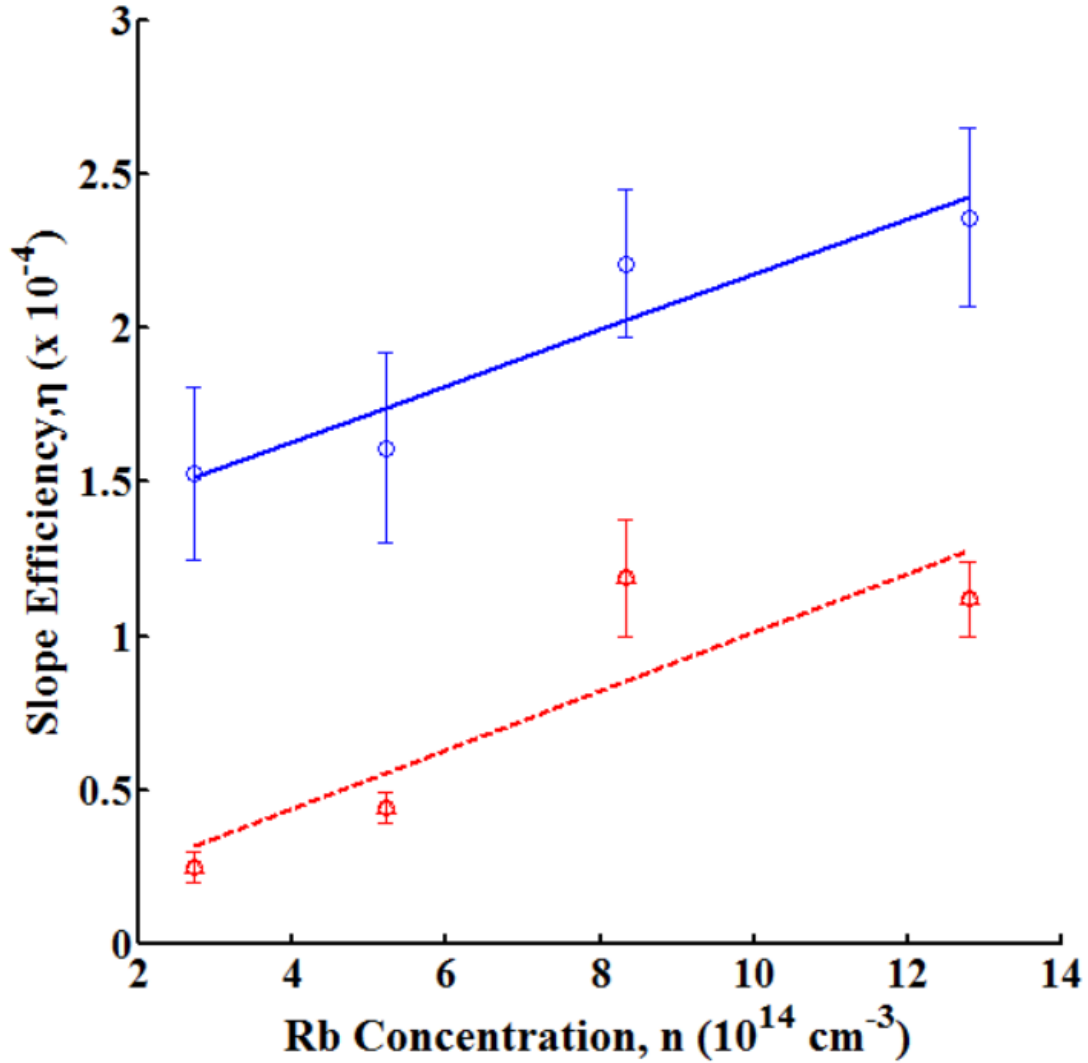


Figure 4.11. Slope efficiency as a function of Rb density for the $6^2P_{1/2} - 6^2S_{1/2}$ (Δ) and $6^2P_{3/2} - 6^2S_{1/2}$ (\circ) transitions. Slope efficiency scales linearly with increasing Rb density for both transitions. It is likely that any appearance of rollover was due to the experimental factors described above, and not any physics of the laser.

Figure 4.12 shows threshold pump energy, E_{th} as a function of rubidium concentration for both the $6^2P_{3/2} - 6^2S_{1/2}$ and $6^2P_{1/2} - 6^2S_{1/2}$ transitions. It is clear from Figure 4.12 that E_{th} does not scale linearly with Rb concentration. For the traditional DPAL, stimulated emission photons are re-absorbed by ground state atoms along the D₁ line if the entire cell is not bleached. Thus, the energy required to bleach the cell, and therefore the threshold energy, will increase as the concentration is increased. For the mid-IR Rb laser, lasing photons cannot be re-absorbed by ground state atoms, so E_{th} will not grow linearly with concentration, as confirmed by experiment.

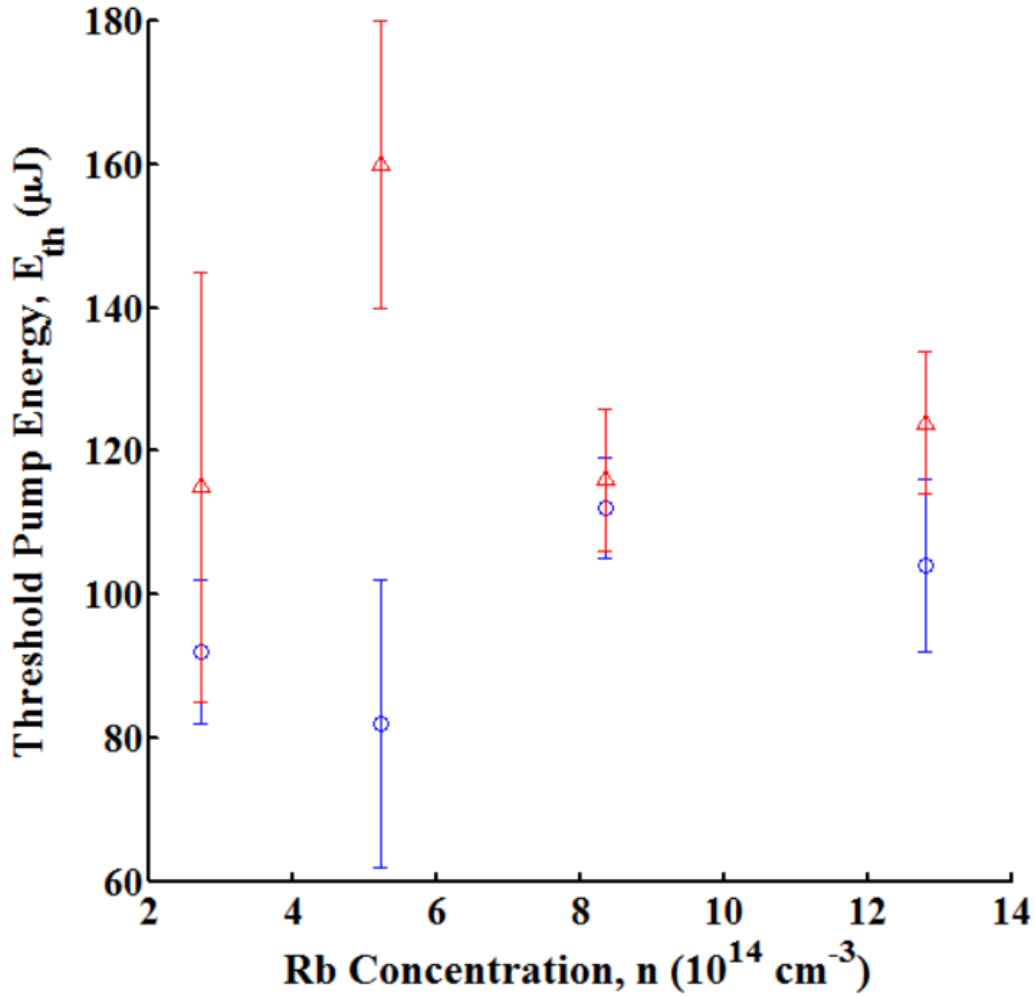


Figure 4.12. Threshold pump energy as a function of Rb density for the $6^2P_{1/2} - 6^2S_{1/2}$ (Δ) and $6^2P_{3/2} - 6^2S_{1/2}$ (\circ) transitions. E_{th} has no coherent relationship with n .

Rb Laser Output Energy vs. Rb Concentration

Figure 4.13 shows IR output energy per pulse as function of Rb concentration for both the $6^2P_{3/2} - 6^2S_{1/2}$ and $6^2P_{1/2} - 6^2S_{1/2}$ transitions overlaid with the same data from Richards. Pumping occurred at 10 mJ/pulse, well beyond the energy required to bleach the cell at the highest Rb concentration considered ($1.96 \times 10^{15} \text{ cm}^{-3}$).

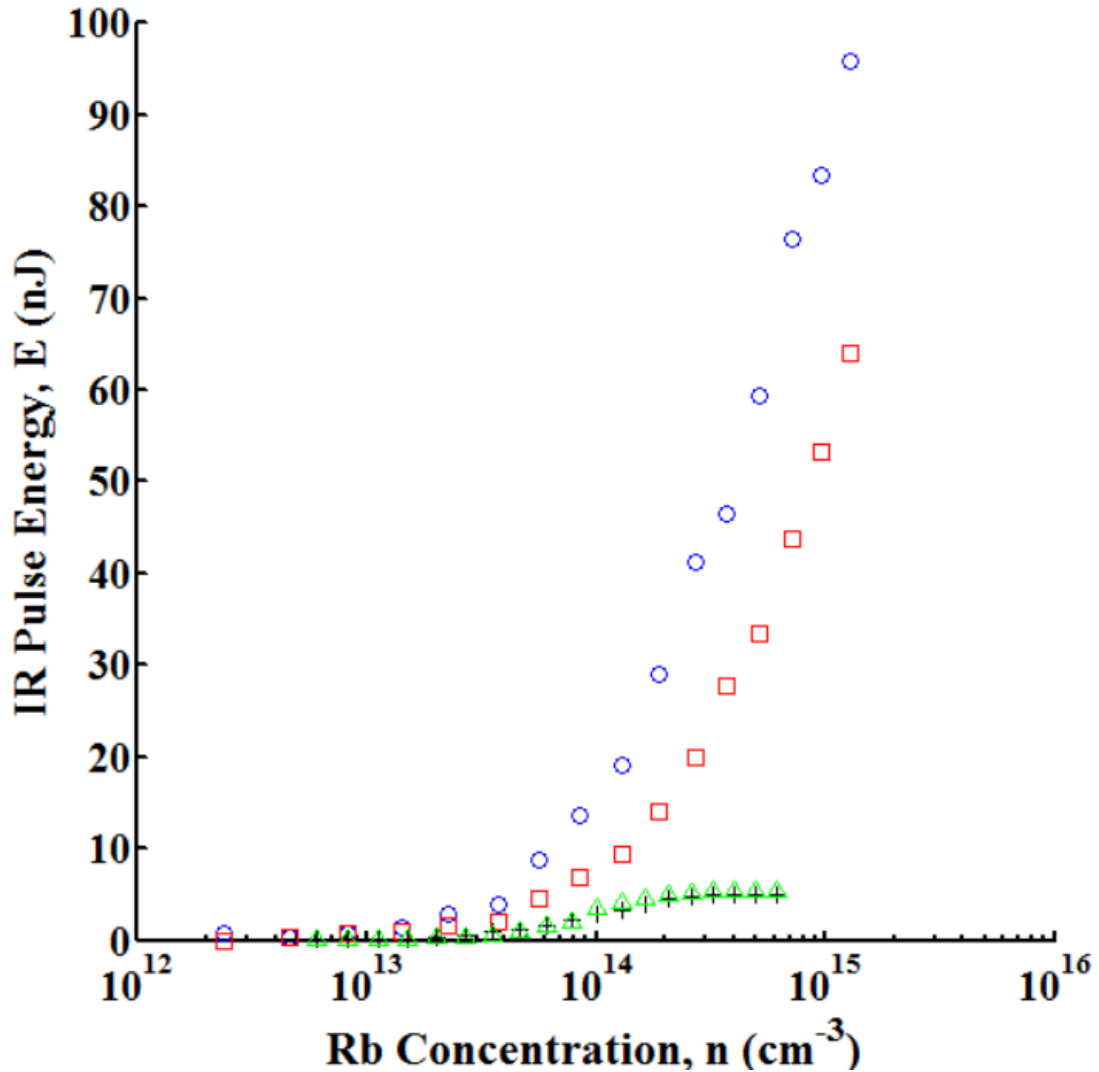


Figure 4.13. IR laser output energy per pulse as a function of Rb density for the $6^2P_{1/2} - 6^2S_{1/2}$ (□) and $6^2P_{3/2} - 6^2S_{1/2}$ (○) transitions with a pump energy of 10 mJ/pulse. Both transitions scale linearly with increasing Rb density. Richards' data for the $6^2P_{1/2} - 6^2S_{1/2}$ (+) and $6^2P_{3/2} - 6^2S_{1/2}$ (Δ) transitions is also shown (Richards, 2013:29).

It can be clearly seen from Figure 4.12 that IR laser energy scales linearly with increasing Rb density for both the 2.73 μm and 2.79 μm transitions. There is no indication of the rollover observed by Richards and Sharma shown in Figure 1.1. This is true well beyond Richards' supposed rollover point and out to the maximum Rb density the heat pipe could maintain. There is no evidence of second-order quantum processes preventing the laser from scaling linearly with increasing Rb density.

These data indicate that rollover should not occur until the number of Rb atoms in the active volume is greater than the number of available pump photons. The heat pipe could not maintain a temperature even close to that needed for the cell to not be completely bleached, but the rollover point could be estimated by comparing the number of Rb atoms available at highest possible concentration to the number of pump photons per pulse. As mentioned above, the number of Rb atoms in the active volume was approximately 2×10^{14} . The number of photons (n_ϕ) in the pump beam is given by Equation 4.9:

$$n_\phi = \frac{E}{h\nu}, \quad (9)$$

where E is the laser energy, h is the Planck constant, and ν is the frequency. At a pump energy of 14 mJ, the 420.2 nm pump beam produces 2.96×10^{16} photons per pulse. From the degeneracy ratio, one-half the atoms Rb atoms are able to be excited to the $6^2P_{3/2}$ state. An active volume with 6×10^{16} Rb atoms could be achieved at a concentration of $\sim 6 \times 10^{17} \text{ cm}^{-3}$, or a heat pipe temperature of $\sim 455^\circ \text{ C}$.

Pulsed Absorption Spectra and Laser Efficiency

The data in Figures 4.6, 4.7, and 4.13 show that the maximum output energy and efficiency of the IR laser could be scaled to a factor of one-to-two orders of magnitude greater than those demonstrated by Richards (Richards, 2013:25). However, these experiments still only demonstrated a maximum laser efficiency on the order of 10^{-4} . This was still several orders of magnitude smaller than the maximum efficiency of the laser. The observed efficiency, $\eta_{observed}$, can be calculated using Equation 4.10,

$$\eta_{observed} = \eta_{quantum} \eta_{absorbed} , \quad (10)$$

where $\eta_{quantum}$, the quantum efficiency of the laser, can be found by dividing the energy difference in eV of the laser transition by the energy difference of the pump transition, and $\eta_{absorbed}$ is the percentage of pump photons absorbed in the active volume. The maximum value of η occurs when all pump photons are absorbed, $\eta_{absorbed} = 1$, and $\eta_{observed} = \eta_{quantum}$.

For the traditional DPAL, the pump and laser energies are very close and the quantum efficiency is therefore very high. The quantum defect is much lower for the mid-IR Rb laser at 6.62% for the $6^2P_{1/2} - 6^2S_{1/2}$ transition and 6.50% for the $6^2P_{3/2} - 6^2S_{1/2}$ transition. The maximum observed slope efficiency of $\sim 2 \times 10^{-4}$ was still $\sim 0.3\%$ of the maximum efficiency of the laser.

To estimate of $\eta_{absorbed}$, a pulsed absorption spectrum, shown in Figure 4.14, was collected using the setup shown in Figure 3.7. A dye laser output of 10 mJ was attenuated by an OD-3.0 ND filter ahead of the heat pipe, giving a pump energy of $\sim 10 \mu\text{J}$. The pump energy had to be sufficiently small that the off-resonance absorption could be differentiated from the on-resonance. When the dye laser was on-resonance, the above-baseline intensity recorded by the Ocean Optics

spectrometer was smaller than the off-resonance intensity by 2.5 percent at 420.2 nm and 1.9 percent at 421.7 nm. This indicated that even for a very small pump energy of 10 μ J, only about 2-3 percent of the pump photons were absorbed.

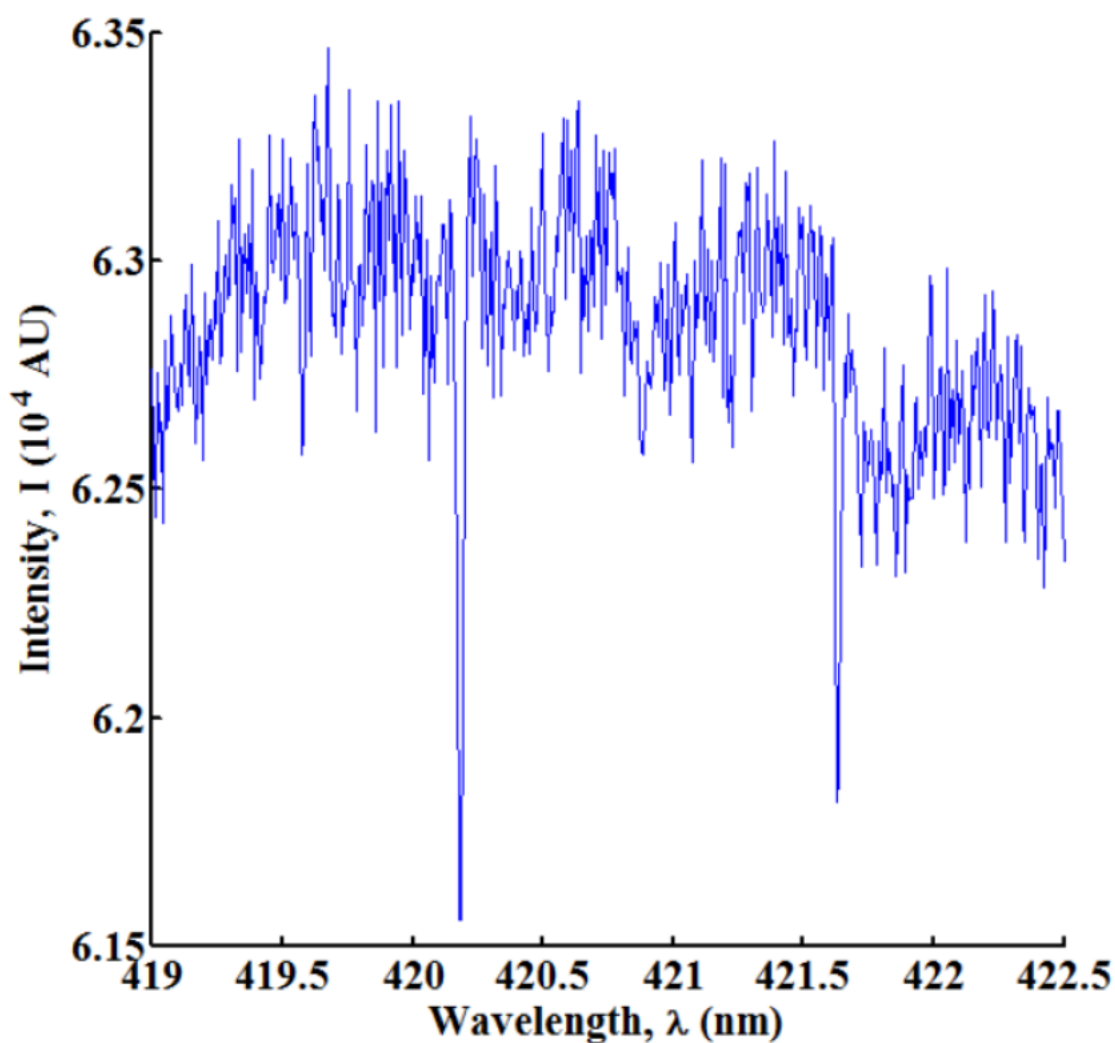


Figure 4.14: Pulsed absorption spectra. The intensity of the unabsorbed pump photons was measured by a spectrometer and plotted against dye laser wavelength. The two dips in intensity occurred at the two lasing transitions. There was a 2.5 percent difference in on- and off-resonance counts above baseline (~ 900 AU) for the 420.2 nm transition, and a 1.9 percent difference for the 421.7 nm transition.

Several conclusions can be drawn from the data presented in Figure 4.14. Most importantly, this data suggests that a very small percentage ($\ll 1\%$) of the pump photons were absorbed at the pump energies ($\sim 100 \mu\text{J}$ – 14 mJ) at which the dye laser operated in the scaling experiments. This indicates that the small laser efficiencies reported by Richards (Richards, 2013:25) and in this thesis (see Table 4.4) were due not to physical phenomena, as Sharma hypothesized (Sharma, 1981:211), but were due instead to the number of pump photons far exceeding the number of excitable Rb atoms in the gain cell. For the $5^2\text{S}_{1/2} - 6^2\text{P}_{3/2}$ (420.2 nm) pump transition (for which the degeneracy ratio = 2:1), a 2.5% difference in on- and off-resonance intensity meant that there were 5% as many Rb atoms as there were pump photons at a pump energy of $10 \mu\text{J}$. This meant that at $E_{\text{pump}} = 10 \text{ mJ}$, there were $\sim 20,000$ pump photons per pulse for each excitable Rb atom in the gain volume!

The data shown in Figure 4.14 also raises some troubling questions. First, the pump energy in this experiment, $\sim 10 \mu\text{J}$, was below the values of E_{th} reported in Table 4.4 and Figure 4.12 by nearly an order of magnitude. As mentioned above, the noise threshold of the power meter used to measure E_{pump} was $\sim 0.5 \text{ mJ}$. Therefore, it is likely that bleaching and threshold occurred at much smaller values of E_{pump} , which could not be detected by the power meter used. It is also possible that the OD-3.0 ND filter did not fully attenuate the beam by a factor of 10^3 ; as the noise threshold of the visible power meter was $\sim 0.5 \text{ mJ}$, the power of the attenuated beam could not be verified.

Also, the number of atoms that should be in the gain volume based on the data from Figure 4.14 does not match the number of atoms predicted from the concentration. Using Equation 4.9, a pump energy of $10 \mu\text{J}$ corresponds with $\sim 3 \times 10^{13}$ photons/pulse. Assuming 2.5% of these photons were absorbed and accounting for the degeneracy ratio, the data indicate that there were only about 1.5×10^{12} atoms in the gain volume. This experiment was performed at a heat pipe temperature of

215° C, or a concentration of $1.6 \times 10^{15} \text{ cm}^{-3}$. Assuming a path length of 10 cm and a spot area of 1 mm^2 , there should have been $1.6 \times 10^{14} \text{ cm}^{-3}$ atoms in the gain volume. Several factors could have contributed to this difference. As discussed earlier in this chapter, there was significant uncertainty in both the gain path length and the pump spot area; it is possible that the gain volume was smaller than the value of 0.1 cm^3 used for this calculation. Additionally, the temperature at the center of the cell may have been colder than the temperature of the thermocouple at the cell edge, which would correspond with a smaller concentration. Also, as mentioned above, the beam may not have been attenuated by a smaller amount than 10^3 . It is also possible that the two absorption features shown in Figure 4.14 were diminished, either because the tuning speed (10 pm/s) was too fast, or because of the large bandwidth of the dye laser ($\sim 2 \text{ GHz}$). The number of pulses (10 per second) was also not accounted for; it is possible that the intensity averaged over multiple pulses made the ratio of on- and off-resonance intensities appear larger than it actually was. One or many of these factors may explain the discrepancy in expected Rb concentration.

In spite of these problems, the data from Figure 4.14 provides convincing evidence that the small observed laser efficiency associated with the mid-IR Rb laser was indeed due to a poor matching of pump photons and Rb atoms. If $\eta_{\text{absorbed}} = 2.5\%$ at $E_{\text{pump}} = 10 \text{ } \mu\text{J}$, the efficiency on an absorbed photon basis, η , was 0.68%, or $\sim 10\%$ of the maximum possible efficiency, $\eta_{\text{quantum}} = 6.5\%$. The efficiency on an absorbed photons basis may have been even higher, approaching η_{quantum} , depending on the actual E_{pump} at which linear growth occurred in the scaling curves shown in Figures 4.5 and 4.6. As mentioned above, this was not possible to determine with the power meter used to measure E_{pump} in these experiments. Recommendations for future work include performing the energy scaling experiments again with a more appropriate power meter. This would provide a better estimate of η , η_{absorbed} , and E_{th} (see Chapter V).

Continuous Wave (cw) Absorption Spectra and cw Laser Attempt

In addition to the experiments using the pulsed pump presented above, additional work was done using a Toptica Photonics BlueTune cw tunable diode laser as the pump. The purpose of the cw work was twofold. The primary goal was to study the spectral features of the pump transitions at greater resolution. Additionally, an attempt was made to demonstrate a cw mid-IR Rb laser in order to replicate and improve upon the work of Sharma. The absorption spectra collected using the setup from Figure 3.8 are shown in Figures 4.15 and 4.16.

Absorption spectra were collected for both transitions at multiple Rb concentrations ranging from $1.07 \times 10^{12} \text{ cm}^{-3}$ to $3.24 \times 10^{14} \text{ cm}^{-3}$ (corresponding to temperatures ranging from 75° C to 175° C). From these spectra, the hyperfine structure of the two transitions was resolved. For both transitions, four peaks, each the superposition of two ($5^2\text{S}_{1/2} - 6^2\text{P}_{1/2}$) or three ($5^2\text{S}_{1/2} - 6^2\text{P}_{3/2}$) hyperfine lines, were resolved. For the $5^2\text{S}_{1/2} - 6^2\text{P}_{1/2}$ (421.7 nm) transition, the central frequencies of the four peaks were at 710.95772 THz, 710.95879 THz, 710.96189 THz, and 710.96463 THz. For the $5^2\text{S}_{3/2} - 6^2\text{P}_{1/2}$ (420.2 nm) transition, the central frequencies were at 713.28176 THz, 713.28296 THz, 713.28584 THz, and 713.28865 THz.

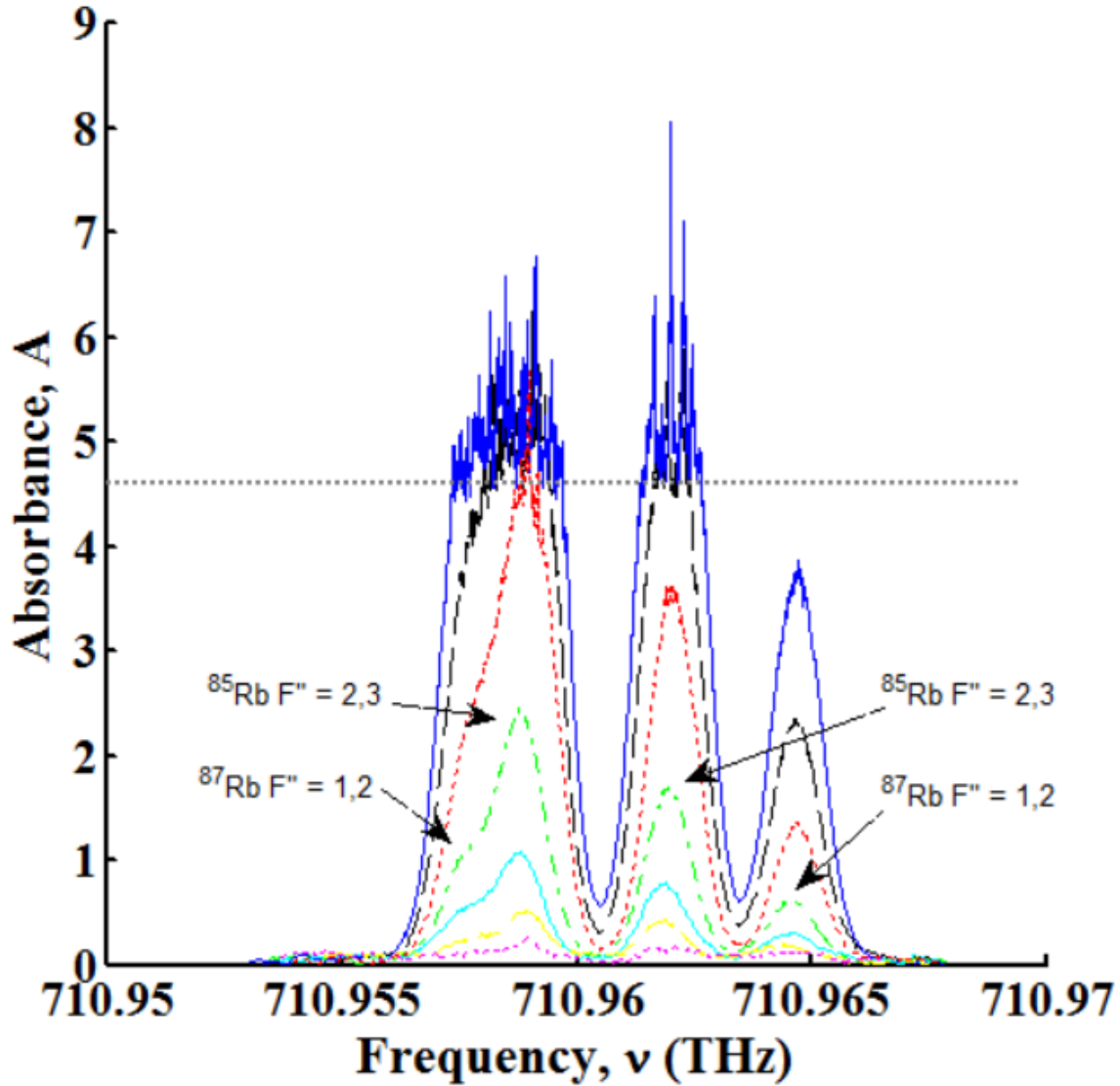


Figure 4.15: Absorption spectra for the $5^2S_{1/2} - 6^2P_{1/2}$ (421.7 nm) pump transition. The spectra were collected at Rb densities of 1.07×10^{12} (—), 4.64×10^{12} (—), 1.43×10^{13} (—), 3.76×10^{13} (—), 8.47×10^{13} (—), 1.88×10^{14} (—), and $3.25 \times 10^{14} \text{ cm}^{-3}$ (—). The cell was completely opaque above an absorbance A of approximately 4.5, as can be seen for the spectra collected at high Rb concentrations. Four peaks, each a superposition of three hyperfine lines, were resolved at central frequencies of 710.95772 THz, 710.95879 THz, 710.96189 THz, and 710.96463 THz.

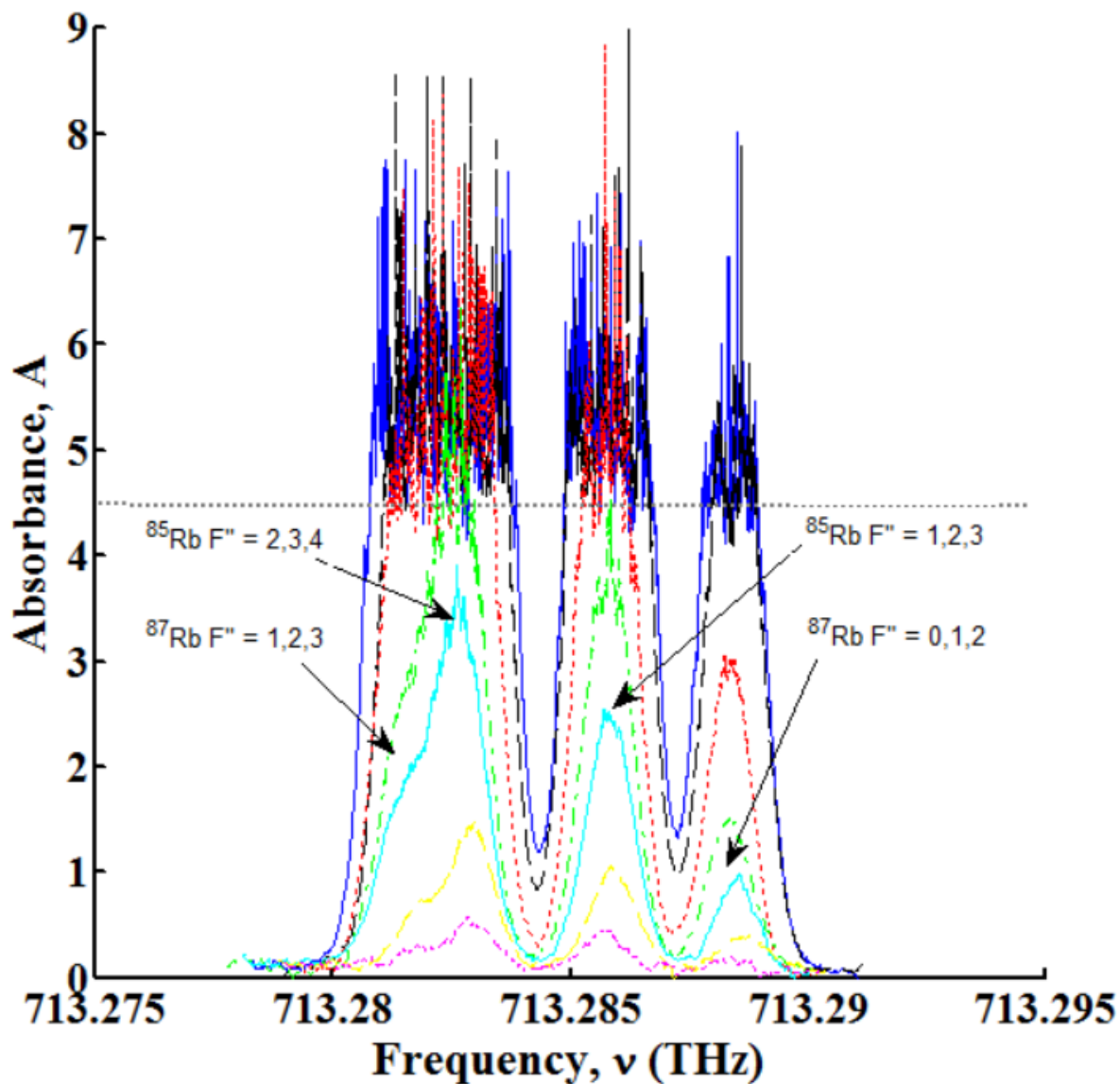


Figure 4.16: Absorption spectra for the $5^2S_{3/2} - 6^2P_{1/2}$ (420.2 nm) pump transition. The spectra were collected at Rb densities of 1.07×10^{12} (—), 4.64×10^{12} (—), 1.43×10^{13} (—), 3.76×10^{13} (—), 8.47×10^{13} (—), 1.88×10^{14} (—), and $3.25 \times 10^{14} \text{ cm}^{-3}$ (—). The cell was completely opaque above an absorbance A of approximately 4.5, as can be seen for the spectra collected at high Rb concentrations. Four peaks, each a superposition of three hyperfine lines, were resolved at central frequencies of 713.28176 THz, 713.28296 THz, 713.28584 THz, and 713.28865 THz.

The data in Figures 4.15 and 4.16 was analyzed in several ways. The maximum value of absorbance was plotted as a function of rubidium concentration for the smaller hyperfine doublet of each isotope for the $5^2S_{1/2} - 6^2P_{1/2}$ transition. These plots are shown in Figure 4.17.

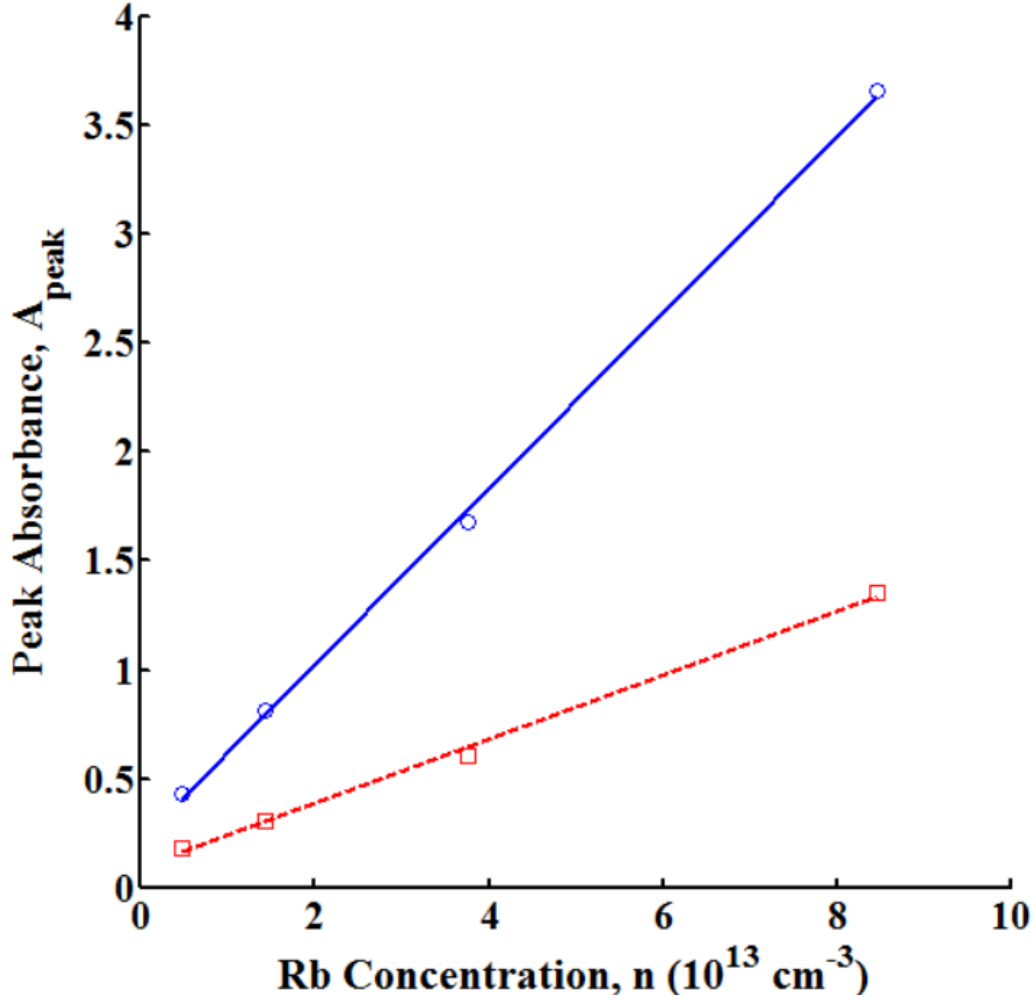


Figure 4.17. Peak absorbance as a function of Rb density for ^{87}Rb (\square) and ^{85}Rb (\circ) for the $6^2P_{1/2} - 6^2S_{1/2}$ transition. The ^{87}Rb line has a slope of $0.1468 / \text{cm}^{-3}$ and the ^{85}Rb line has a slope of $0.403 / \text{cm}^{-3}$. The ratio of these slopes is 2.7:1, equal to the isotopic abundance ratio of 2.7:1.

It should be expected that as the concentration in the cell increases and the pump intensity is held constant, the number of pump photons absorbed will grow. It can be seen from Figure 4.17

that peak absorbance varies linearly with increasing Rb concentration as expected. The ratio of the ^{85}Rb slope to the ^{87}Rb slope is 2.7:1, exactly equal to the ratio of isotopic abundances.

The cw absorption spectra were further analyzed by fitting the absorption features to a theoretical model. The model plotted absorbance ($\alpha = \sigma nl$, where n is the concentration, l is the gain path length, and σ is the cross section) as a function of frequency. Absorption varied with frequency because σ was dependent on lineshape, $g(\nu)$, and the hyperfine splitting. Figure 4.18 shows the theoretical and experimental absorption spectra at $n = 8.47 \times 10^{13} \text{ cm}^{-3}$ with $l = 10.2 \text{ cm}$.

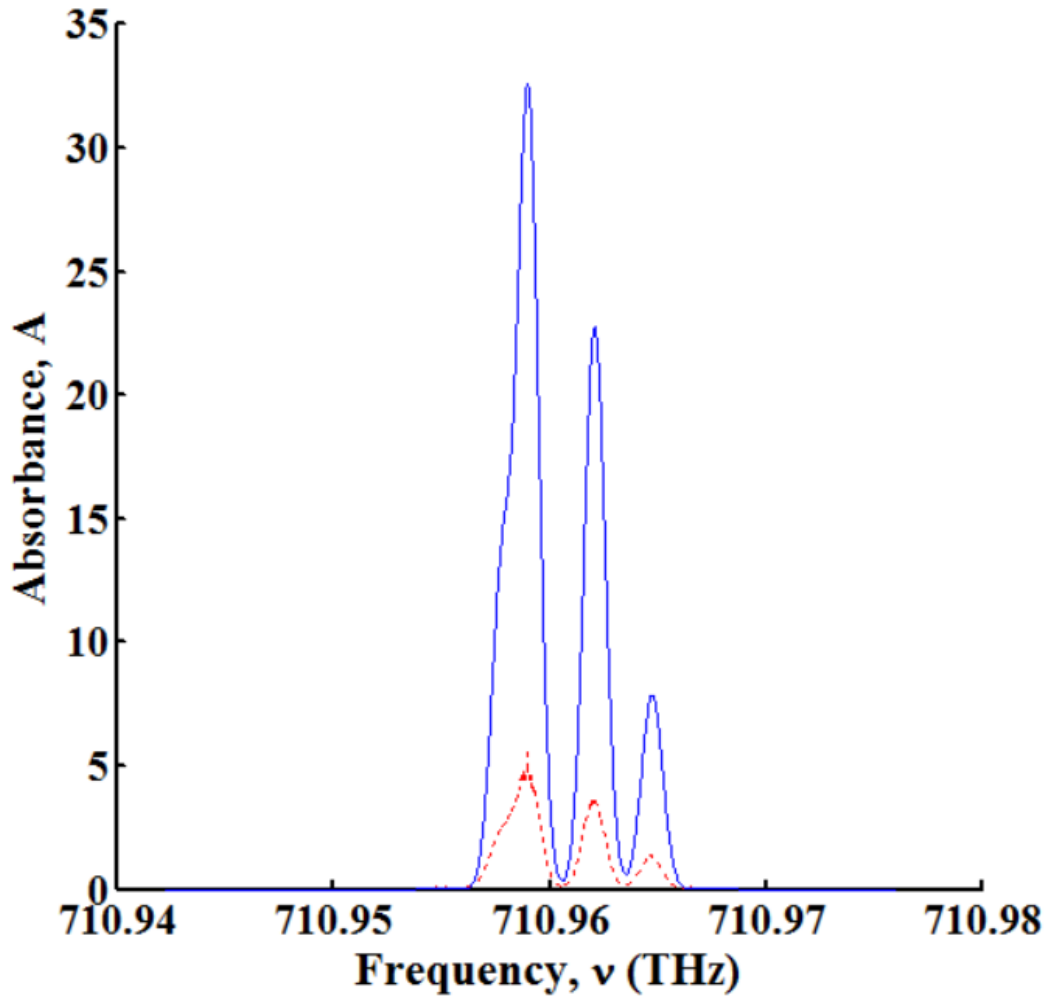


Figure 4.18. Theoretical (—) and experimental (---) cw absorption spectra for the $5^2\text{S}_{1/2} - 6^2\text{P}_{1/2}$ (421.7 nm) transition at $n = 8.47 \times 10^{13} \text{ cm}^{-3}$.

Figure 4.18 shows that the theoretical and experimental values of absorption varied significantly, by a factor of ~ 6 . This could have been due to several factors. As mentioned previously, it is possible that the temperature at the center of the heat pipe was colder than the temperature at the cell edge. For the theoretical model to match the experimental results, the concentration would have to have been a factor of ~ 6 smaller. This would indicate an unlikely large temperature difference of $\sim 30^\circ \text{C}$ from the center to the edge of the cell. Therefore, it is more likely that the cell was only partially bleached, meaning l was smaller than 10.2 cm. The percentage of the cell bleached could be estimated using Equation 4.11,

$$I = I_0 - (\sigma nl)I_s, \quad (11)$$

where I is the laser output intensity, I_0 is the pump intensity, σ is the absorption cross section, n is the Rb concentration, l is the effective gain path length, and I_s is the saturation intensity (Verdeyen, 1989). If $(\sigma nl)I_s > I_0$, the pump intensity would not have been sufficient to bleach the cell entirely. The intensity of the pump beam had a maximum value of $8.68 \times 10^6 \text{ mW/m}^2$. At a Rb concentration of $8.47 \times 10^{13} \text{ cm}^{-3}$, using the value of I_{sat} calculated above of 351.4 mW/m^2 , the $(\sigma nl)I_{sat}$ term was $2.984 \times 10^7 \text{ mW/m}^2$. Thus, $(\sigma nl)I_s > I_0$, indicating that the cell was not entirely bleached.

This hypothesis could be tested by plotting the difference in peak absorption between the theoretical model and experimental results as a function of Rb concentration. Since the pump intensity was held constant, the percentage of the cell bleached should decrease as the concentration is increased. Therefore, the difference between the theoretical and experimental data should increase as concentration grows. This was plotted in Figure 4.19 for the smaller ^{85}Rb doublet of the $5^2\text{S}_{1/2} - 6^2\text{P}_{1/2}$ transition at four different Rb concentrations (4.64×10^{12} , 1.43×10^{13} , 3.76×10^{13} , and $8.47 \times 10^{13} \text{ cm}^{-3}$).

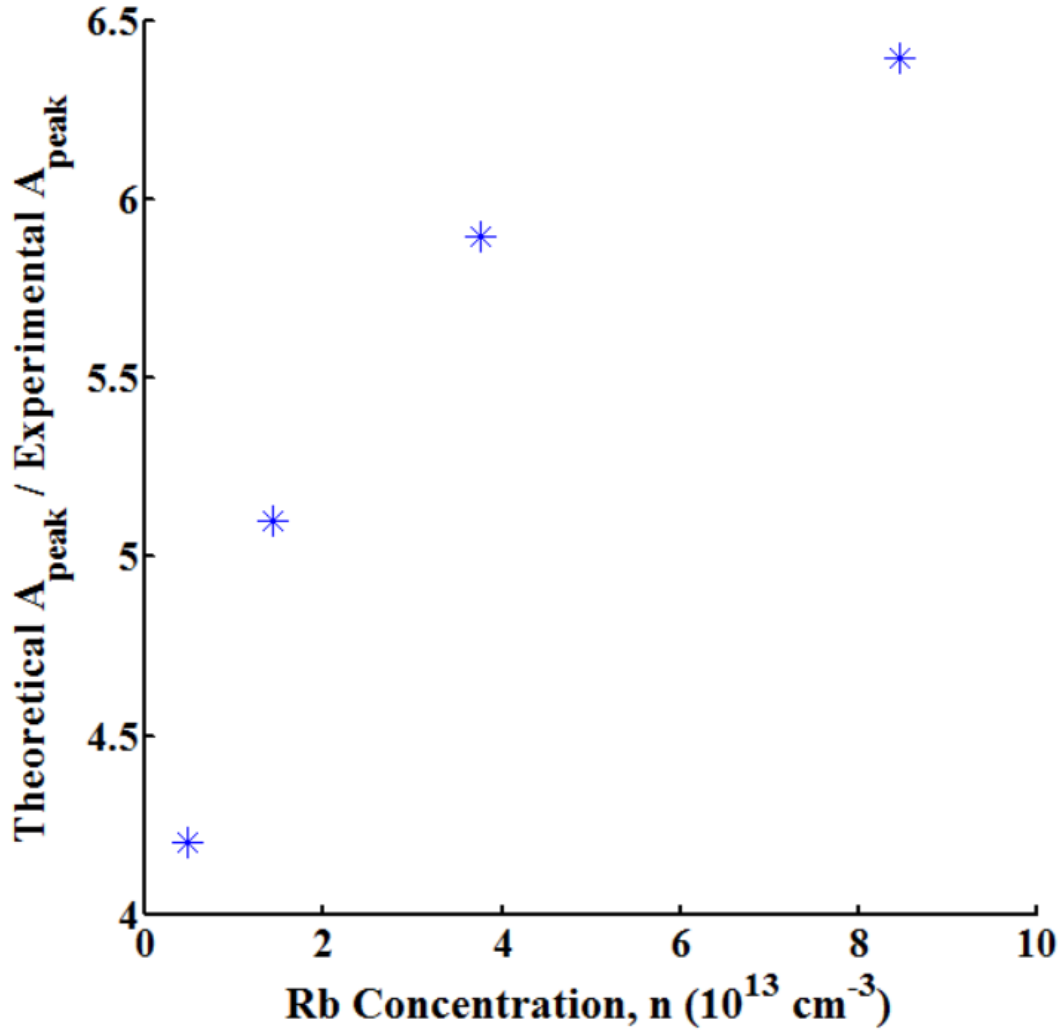


Figure 4.19. Ratio of theoretical peak absorbance to experimental peak absorbance as a function of Rb density. The difference between the theoretical and experimental values grows with n , indicating that a decreasing percentage of the cell was bleached as n increased.

Figure 4.19 shows that the difference between theoretical and experimental A_{peak} increased as concentration grew. This indicates the entire cell was not bleached, as predicted above. Assuming the temperature at the center of the cell was approximately equal to the temperature at the cell edge, only 1.5 cm of the gain path length was bleached at $n = 8.47 \times 10^{13} \text{ cm}^{-3}$. This may explain why the attempt to demonstrate the cw mid-IR Rb laser was unsuccessful. As described in Chapter I, if only a small percentage of the gain cell was bleached, the divergence of the laser

would be large. At $n = 8.47 \times 10^{13} \text{ cm}^{-3}$, using equation 4.3, with $z = 18 \text{ cm}$ (rear window to detector) + 27 cm (edge of l_g to rear window) and $l_g = 1.5 \text{ cm}$, the spot area at the detector was increased by a factor of ~ 1300 ! This is evidence that IR laser signal should not have been observed, and supports the hypothesis that bleaching problems led to the rollover observed by Sharma.

Assumptions, Error, and Uncertainty

Numerous challenges were faced in obtaining the results presented above. The most difficult and most important obstacle was the calibration of the InSb detector. It was critical to convert from oscilloscope signal to laser output energy as accurately as possible. This was made difficult especially by the numerous factors that had to be accounted for, such as the losses on each optic and the ratio of spot sizes, introduced potential sources of error. The number of assumptions required was reduced by instead calibrating with a known source.

Sources of error stemming from the InSb, pre-amp, and oscilloscope included the ringing in the pulse decay curve shown in Figure 3.4. As discussed above, the ringing in the pulse decay curve was a product of the slow pre-amp response time. While the linear mapping of signal ($\text{V} \cdot \text{s}$) to received energy (J) shown in the calibration curves shown in Figures 3.5 and 3.6 indicates integrating over the entire pulse was a valid approach, a better integrated pulse area could have been found if the response curve was an exponential decay. For future work, a pre-amp with a shorter response time would be desirable to obtain a more accurate measurement of pulse energy. Also, a power meter with a lower noise threshold could be used to better estimate E_{th} and η .

Errors also arose from the pump laser. It was very difficult to hold conditions exactly constant. The short lifetime (15 min half-life) of Stilbene 420 caused the laser dye to degrade

substantially over time, even on the timescale of a single experiment. It was thus impossible to maintain a constant pump energy, though the dye was changed frequently to obtain the best possible result. The pulse-to-pulse energy would vary, especially near threshold, by ± 0.1 - 0.4 mJ/pulse. To resolve this, the signal on the detector was averaged over a large number of traces (1000), but the averaging could only be so long before it was affected by the degradation of the dye. This variation in pump energy, along with the noise threshold of ~ 0.5 mJ of the Coherent power meter, had a major impact on the measurement of IR laser energy near laser threshold. Although the data appear in good agreement with the energy scaling curve fits, the accuracy of the energy measurements near lasing threshold is questionable. This would also impact the accuracy of the measured slope efficiencies. The uncertainty of the pump energy below 0.4 mJ may have affected the efficiencies observed in this experiment, as well as Richards'.

Although it has been discussed at length above, it is worth mentioning again that the spot size of the pump beam had a significant effect on the results obtained. Uncertainty in the active area of the pump beam and the effective gain path length impacted the accuracy of the calculations of active volume. The number of Rb atoms in this volume was also difficult to assess, as the temperature of the heat pipe would fluctuate by $\pm 2^\circ$ C. Moreover, it was assumed that the temperature reported by the Watlow heater controller was equivalent to the temperature inside the cell, which was not necessarily correct. It is possible that temperatures inside the cell were $\sim 10^\circ$ C colder than the temperature at the surface. This would mean that the concentrations in the cell were smaller than believed. The combination of the true values of Rb concentration and active volume being smaller than the reported values might also factor in to a better understanding of the laser efficiency.

V. Conclusion

Conclusions and Discussion

The most significant achievement of this work was the improvement upon and correction of data from experiments conducted by Richards in 2013. Richards reported a maximum output energy of <5 nJ per pulse with a 10 mJ pump. In this work, a maximum laser output of nearly 100 nJ was demonstrated with the same pump energy, an improvement in laser efficiency on the order of 100. Additionally, experiments were conducted which suggested that the pump energy in the pulsed experiments was far greater than required to bleach the cell, resulting in an absorption efficiency $\eta_{absorbed}$ of 0.2 or less. This suggested that the maximum efficiency of the laser could be scaled to efficiencies much greater than those reported by Richards, possibly approaching the quantum efficiency of approximately 6.5 percent.

Richards' data indicated a rollover in IR laser output energy and bleached limit above an Rb concentration of approximately 2.5×10^{14} . If true, this would prohibit the laser from being scaled to energies required for any practical application. It was shown conclusively that both output energy and bleached limit scale linearly with increasing concentration, with linear scaling to concentrations an order of magnitude larger than Richards' supposed rollover point.

These results suggest that the mid-IR Rb laser may indeed be useful for practical defense applications. This laser offers several attractive properties for a variety of Air Force missions. At 2.7 μm , the laser wavelength is desirable for many laser weapons missions (Traub, 1976:369). Another benefit is the possibility of wavelength agility and cascade lasing. Ideally, a laser incorporated into an IR-CM system would be tunable over a wide band of wavelengths. Although the laser demonstrated here only operates at two wavelengths, a mid-Rb IR laser system could

achieve greater wavelength diversity by cascade lasing. Sharma observed cascade lasing along the $6S_{1/2}$ - $5P_{3/2}$ and $6S_{1/2}$ - $5P_{1/2}$ transitions at 1.36 μm (with 40 percent relative intensity compared to the 6P-6S transition) and 1.32 μm (30 percent relative intensity), respectively. Cascade laser action continued out of the 5P states along the D₁ and D₂ lines (780 and 795 nm) at 10 percent relative intensity compared to the 6P-6S transition. The 6S-5P and 5P-5S transitions have decay lifetimes of 80 ns ($6S_{1/2}$ - $5P_{3/2}$), 160 ns ($6S_{1/2}$ - $5P_{1/2}$), 26 ns ($5P_{3/2}$ - $5S_{1/2}$), and 28 ns ($5P_{1/2}$ - $5S_{1/2}$), all of which are faster than the decay time of the 6P-6S transitions of ~ 220 ns. Therefore, bottlenecking should not limit cascade laser performance. Sharma observed that Rb atoms pumped to the 6P states also lase to the 4D states at 2.25 μm with relative strengths compared to the 6P-6S transitions of 0.60 ($6P_{3/2}$ - $4D_{3/2}$) and 0.30 ($6^2P_{1/2}$ - $4D_{5/2}$). Cascade lasing in the mid-IR Rb laser system offers further wavelength diversity and better efficiency, as the combined output energies of the 6P-4D, 6S-5P and 5P-5S are approximately equal to the output energy from the 6P-6S laser. Further wavelength agility could be achieved by two-photon absorption to the 5D and 7S energy levels (Brown, 2013:51), as well as the 7P states. Immediate future work on this system should place an emphasis on studying cascade lasing effects and alternative pump wavelengths for the pulsed mid-IR Rb laser.

A great deal of work remains before the mid-IR Rb laser is system capable; ideas for future steps toward that goal are discussed below. In spite of these challenges, the major impact of this work was to show that the physics of this laser scheme do not prevent scaling to practically useful energies, and that the mid-IR Rb laser may indeed be incorporated into a future Air Force system.

Recommendations for Future Work

As mentioned above, any work on the mid-IR Rb laser immediately following this thesis should concentrate on studying cascade lasing effects. If cascade lasing is demonstrated at appreciable relative intensities compared to the lasing 6P-6S transition, the total efficiency and wavelength agility of the laser would increase significantly. This would make the mid-IR Rb laser more desirable for incorporation into an IR-CM system.

Another obvious step in any future work on the mid-IR Rb laser must be to scale the laser efficiency to near $\eta_{quantum}$. This will require a large increase the Rb concentration in the heat pipe, so that the number of excitable Rb atoms approaches the number of pump photons. Based on the data presented in Figure 4.13, there is no indication of the rollover in output energy reported by Richards, indicating that the efficiency of the laser should continue to grow linearly with increasing Rb concentration. To scale the laser to higher efficiency, the Rb concentration in the heat pipe must be increased well beyond the maximum concentration considered here. How laser output energy is affected by heat pipe conditions above $\sim 225^{\circ}\text{C}$, such as by the formation of alkali dimers (Fayet, 1986), must be explored.

Additionally, the spectral width of the pump transition must be broadened to accept the relatively broadband output of commercially available blue diode pump sources. If the pump transition is broadened appropriately, output powers in excess of 1 kW (Bogachev, 2012:95) could be achieved by pumping with a diode stack. However, Richards showed that the addition of various buffer gases, including argon, ethane and helium, quenched laser action very quickly (Richards, 2013:30). Thus, an immediate challenge would be to find a buffer gas that will broaden the pump transition without quenching laser action.

It would also be beneficial to replicate some of the work presented here with improved equipment. A power meter with a lower noise-threshold would improve the accuracy of the energy scaling data obtained, especially at low pump energies. This would likely reveal the pump energies near threshold were actually lower than indicated by the Coherent power meter, and would allow the values of threshold and slope efficiency to be measured with greater confidence. Additionally, a better understanding of the conditions in the heat pipe, specifically the temperature at center as opposed to the exterior of the cell and the true effective gain path length, would improve confidence in the efficiency reported here. A pump source with a much higher beam quality than the dye laser would lead to a better estimate of the active volume in the heat pipe as well.

Furthermore, it would be beneficial to make a second attempt at demonstrating the cw mid-IR Rb laser using a higher power pump source or a cell with a smaller path length. With a sufficiently high power pump laser, the gain cell could be entirely bleached, and Sharma's results could be reproduced. It could be seen if higher efficiency and linear scaling with increasing Rb concentration could be demonstrated for the cw mid-IR Rb laser, as was done for the pulsed case.

Bibliography

- D. Aumiler, T. Ban, and G. Pichler. "High-resolution measurements of the pressure broadening and shift of the rubidium $5 S_{1/2} - 6 P_{3/2}$ line by argon and helium," *Physical Review A*, **70**, 032723 (2004).
- G.H. Bearman and J.J. Leventhal, "Ionization and Energy Pooling in Laser-Excited Na Vapor," *Physical Review Letters* **41**, 1227-1230 (1978).
- P.F. Bernath, *Spectra of atoms and molecules*. Oxford University Press, (2005).
- A.V. Bogachev, and others, "Diode-pumped caesium vapour laser with closed-cycle laser-active medium circulation." *Quantum Electronics* **42**, No. 2, 95-98, (2012).
- V.M. Borodin, A.N. Klyucharev, and V. Yu, "Associative ionization of excited 5^2P rubidium atoms", *Optics and Spectroscopy* **39**, 231-232 (1975).
- K.C. Brown, and G.P. Perram. "Demonstration of a 459-nm pulsed, optically pumped cesium vapor laser." *Optics Communications* **300**, 51-57 (2013).
- S.A. Clough, and others, "Atmospheric radiance and transmittance-FASCOD2," *6th Conference on Atmospheric Radiation*. **1**, 141-144 (1986).
- W. Demtröder. *Laser Spectroscopy*. **4**, Berlin, Heidelberg, Springer, (1982).
- E.L. Dereniak, and G.D. Boreman. *Infrared Detectors and Systems*. Wiley, 1996.
- P. Fayet, J.P. Wolf, and L. Wöste. "Temperature measurement of sputtered metal dimers." *Physical Review B*, **33**, No. 10, 6792 (1986).
- J.P. Gordon, H.J. Zeiger, and C.H. Townes. "Molecular Microwave Oscillator and New Hyperfine Structure in the Microwave Spectrum of NH_3 ", *Physical Review Letters*, **95**, 282-284 (1954).
- G.D. Hager, and G. P. Perram. "A three-level analytic model for alkali metal vapor lasers: part I. Narrowband optical pumping." *Applied Physics B* **101**, No. 1-2, 45-56 (2010).
- W. Klennert, "Development of a Compact Heat Pipe Oven for Optically Pumped Alkali Laser Research," *Journal of Directed Energy* **4**, No. 4 (2012).
- H.R. Kratz and J.E. Mack, "Long optical paths of large aperture," *Journal of the Optical Society of America*, **32**, 285 (1942).
- W.F. Krupke, "Diode pumped alkali lasers (DPALs): an overview," *High-Power Laser Ablation 2008*. International Society for Optics and Photonics, 700521 (2008).

W.F. Krupke and others, "New Class of CW High-Power Diode-Pumped Alkali Lasers (DPALs)," *Proceedings SPIE*, **5448**, 7-17 (2004).

W.F. Krupke, and others, "Resonance Transition 795-nm Rubidium Laser," *Optics Letters*, **28**, No. 23, 2336-2338 (2003).

T.B. Lucatorto and T.J. McIlrath, "Laser Excitation and Ionization of Dense Atomic Vapors," *Applied Optics*, **19**, No. 23, 3948-3956 (1980).

Pandey, Rajiv, and others, "Advancements in high-power diode laser stacks for defense applications," *SPIE Defense, Security, and Sensing*. International Society for Optics and Photonics (2012).

G.P. Perram, and others, *An Introduction to Laser Weapon Systems*. Directed Energy Professional Society (2010).

P. Polak-Dingels, J. F. Delpech, and J. Weiner, "Observation of structure in laser-induced Penning and associative ionization in crossed-beam Na+ Na collisions," *Physical Review Letters* **44**, No. 25, 1663 (1980).

P. Rabinowitz, S. Jacobs, and G. Gold, "Continuous Optically Pumped Cs Laser," *Applied Optics* **1**, No. 4, 513-516 (1962).

R.M. Richards, *Mirrorless Lasing in Optically Pumped Rubidium Vapor*, MS thesis, AFIT-ENP-13-M-41, School of Engineering and Management, Air Force Institute of Technology (AU), Wright-Patterson AFB OH (2013).

A. Sharma, "Continuous-Wave Mirrorless Lasing in Optically Pumped Atomic Cs and Rb Vapors," *Applied Physics B* **39**, No. 3, 209-211 (1981).

Shiner, A. D., and others, "Absolute optical frequency measurement of saturated absorption lines in Rb near 422 nm." *Applied Physics B* **89**, No. 4, 595-601 (2007).

P.P. Sorokin and J.R. Lankard, "Infrared Lasers Resulting from Giant Pulse Laser Excitation of Alkali Metal Molecules," *J. Chem. Phys* **51**, No. 7, 2929-2931 (1970).

C.V. Sulham, G.A. Pitz, and G.P. Perram, "Blue and Infrared Stimulated Emission from Alkali Vapors Pumped through Two-Photon Absorption," *Applied Physics Letters*, **101**, No. 1-2, 57-63 (2010).

W.A. Traub and M.T. Stier, "Theoretical atmospheric transmission in the mid- and far-infrared at four altitudes," *Applied Optics*, **15**, 364-377 (1976).

K, Tsipis. "Laser weapons." *Scientific American* **245**, 51-57 (1981).

J.T. Verdeyen, *Laser Electronics*, Prentice Hall, 640 (1989).

Appendix

This appendix includes additional figures and tables referenced in the text above. Figure A.1 shows Richards' plot of bleached limit as a function of Rb concentration, which corresponds with the plot of bleached limit shown in Figure 4.10. Richards reported a rollover in bleached limit at a Rb concentration of $2.5 \times 10^{14} \text{ cm}^{-3}$. The data in Figure 410 clearly show this rollover to be false.

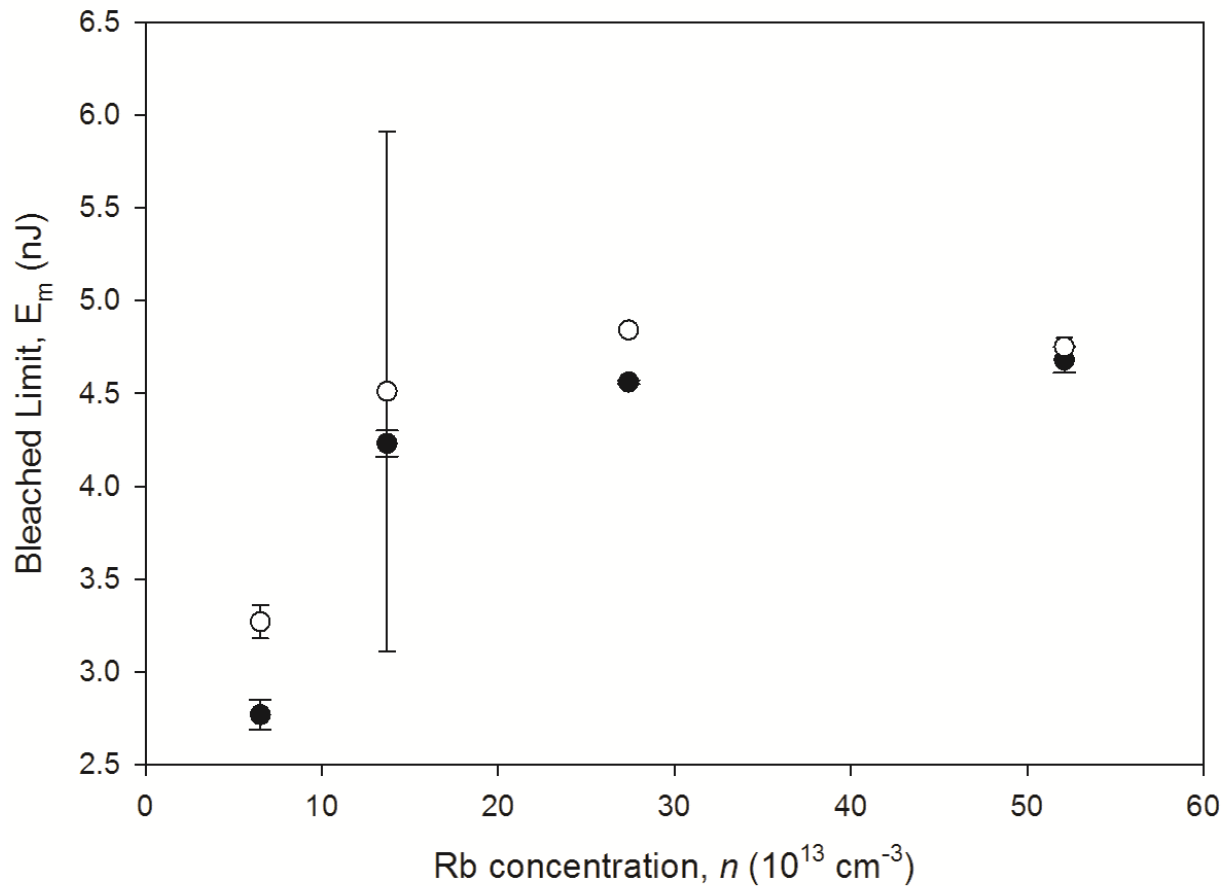


Figure A.1. Figure from Richards showing bleached limit as a function of Rb concentration. The black (●) and white (○) circles represent the 2.73 μm and 2.79 μm transitions. Richards observed a rollover in bleached limit at a Rb concentration $n \sim 2.5 \times 10^{14} \text{ cm}^{-3}$ (Richards, 2013:27).

Figure A.2 shows Richards' plot of slope efficiency vs. Rb concentration, corresponding with the plot of slope efficiency shown in Figure 4.11. Richards' maximum slope efficiency was on the order of 10^{-5} , far lower than the quantum efficiency of 6.5 percent. Additionally, Figure A.2 shows that Richards observed a rollover in slope efficiency of the 2.73 μm transition at a Rb concentration of $2.5 \times 10^{14} \text{ cm}^{-3}$. The data presented in Figure 4.11 show that, like bleached limit, slope efficiency increases linearly with n . Additionally, the results of the pulsed absorption spectroscopy experiment presented in Figure 4.14 show that the small efficiency was the result of the number of pump photons far exceeding the number of excitable atoms, and that the laser was nearly quantum-efficient on an absorbed photon basis.

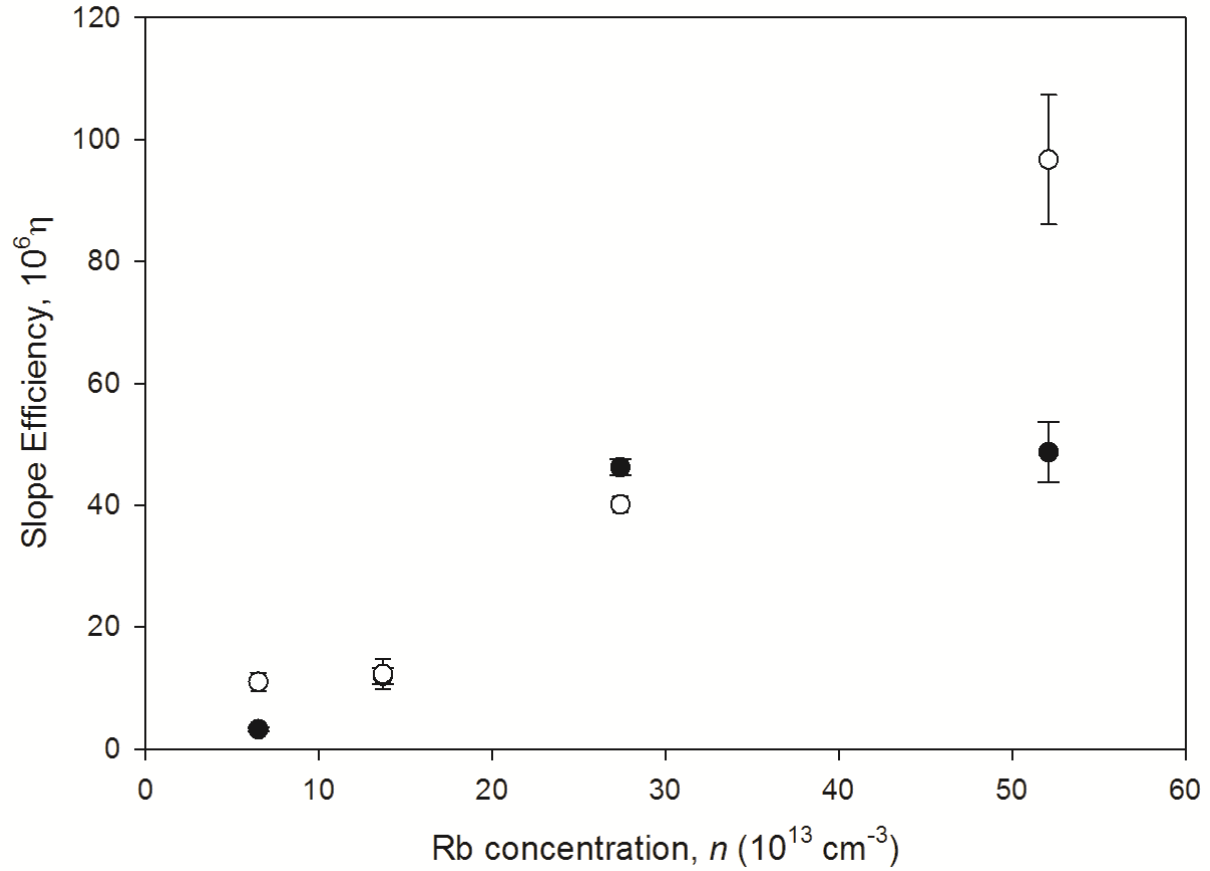


Figure A.2. Richards' plot of slope efficiency vs. Rb concentration. The black (●) and white (○) circles represent the 2.73 μm and 2.79 μm transitions (Richards, 2013:28).

Figure A.3 shows Richards' calibration curve. The large rollover in oscilloscope output as a function of incident blackbody power is evidence that Richards' results were impacted by detector saturation. Richards assumed that all of the measurements made in his work fell on the straight line (near the y-axis). However, in light of the results presented in this thesis, this assumption was shown to have been incorrect.

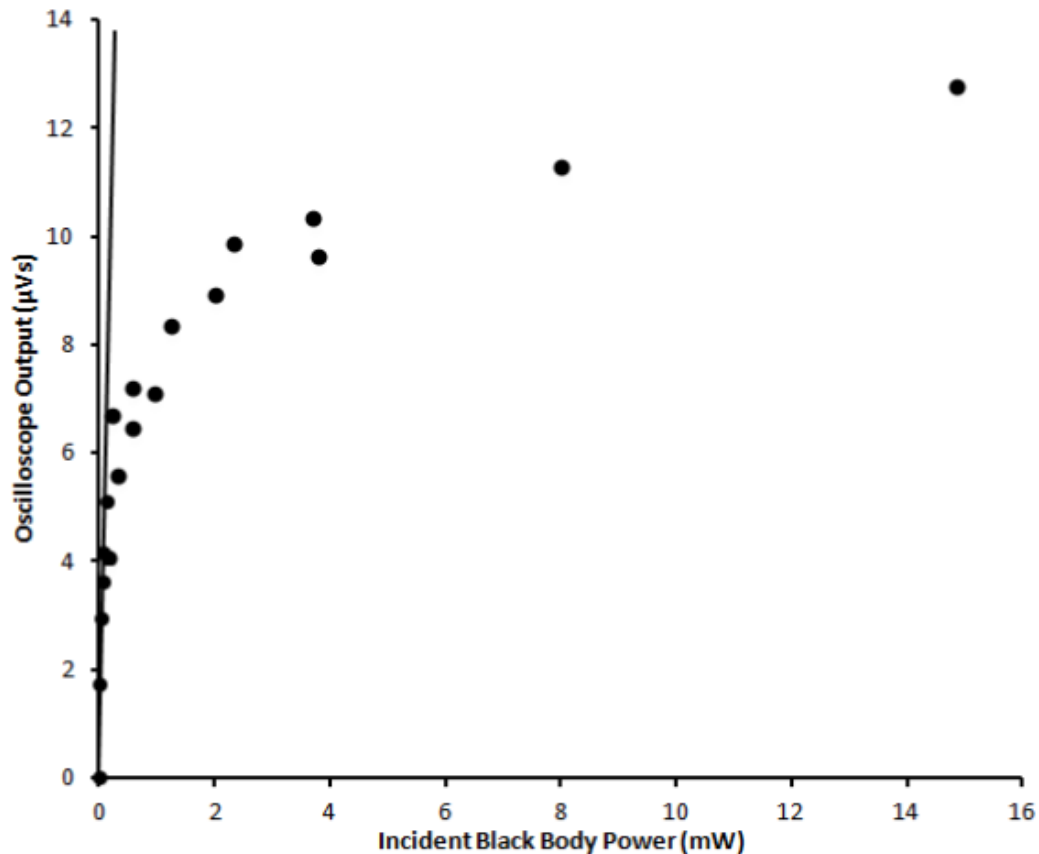


Figure A.3. Richards' blackbody calibration curve. Richards used the solid line to relate oscilloscope output ($\mu\text{V}\cdot\text{s}$) to radiometric power received by the detector. It is obvious that this fit line does not accurately represent Richards' calibration data. Richards, likely based on Sharma's results, assumed the laser's maximum output would be ~ 5 nJ. This led to the assumption that his data would fall within the linear region of the calibration curve. However, based on the data used to make this calibration curve (Richards, 2013:19) and Equation 3.2 (the same equation Richards used), it is likely that Richards made in error in calculating radiometric power received by the detector (Richards, 2013:18).

Figure A.4 shows the oscilloscope signal (V) when the calibration source was both blocked and unblocked. This figure was used to compute the peak-to-peak voltage, which was compared to the received power, and used to convert the area of the pulse decay curve (Vs) to laser output energy (J). The peak-to-peak method was used for both the blackbody calibration and the Daylight Solutions calibration described in Chapter III.

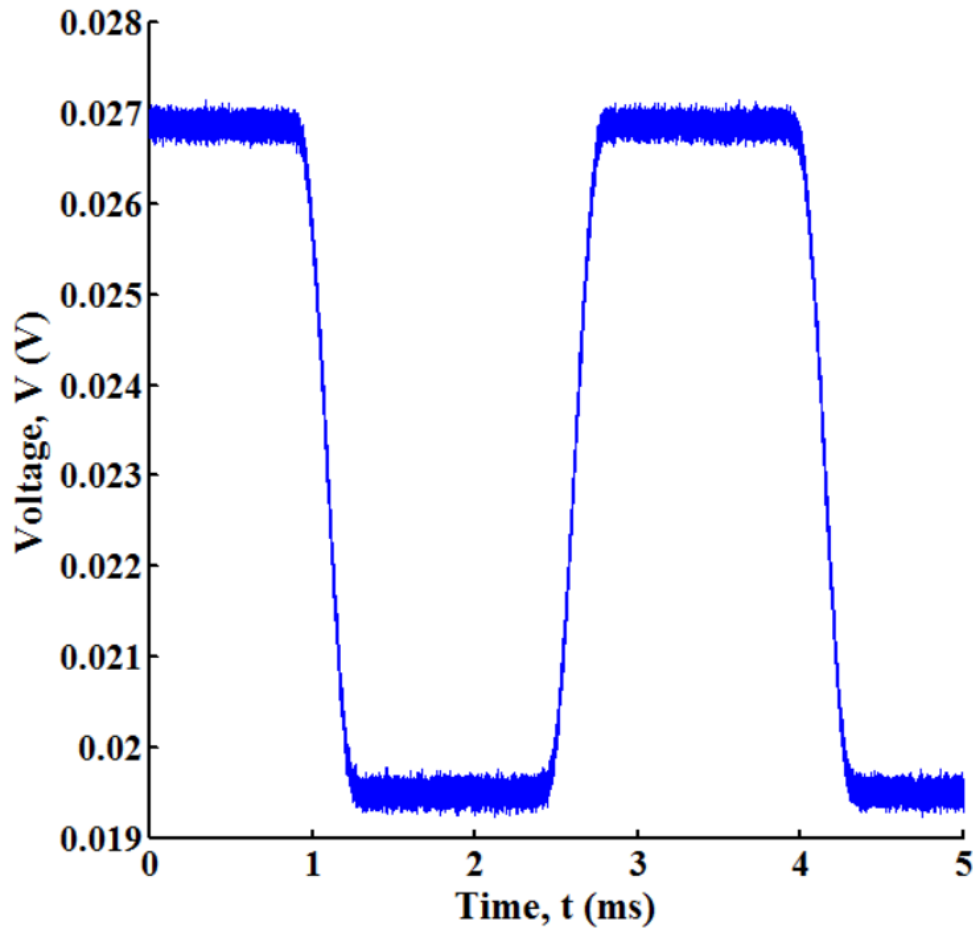


Figure A.4. Oscilloscope voltage received (V) when the calibration signal was both blocked and unblocked. The flat portions of the signal curve were averaged, and the blocked voltage was subtracted from the unblocked voltage to remove background signal. The same peak-to-peak method was used for both the blackbody calibration and the Daylight Solutions calibration. The resulting signal produced solely by the calibration source was converted to energy using the calibration curves shown in Figures 3.5 and 3.6.

Tables A.1, A.2, and A.3 show a verification of the attenuation ratios of the OD-0.5, OD-1.0, and OD-2.0 neutral density filters, respectively. The oscilloscope signal (nVs) was found in both the attenuated and unattenuated cases. The unattenuated signal was divided by the attenuated signal to find the attenuation ratio. This was done at multiple heat pipe temperatures.

Table A.1. Verification of Attenuation Factor of OD-0.5 ND Filter

Heat Pipe Temp	Unattenuated Signal	Attenuated Signal, OD-0.5	Attenuation Ratio
60° C	0.119 nVs	0.026 nVs	4.58
90° C	0.740 nVs	0.177 nVs	4.20
120° C	2.035 nVs	0.404 nVs	5.04

Table A.2. Verification of Attenuation Factor of OD-1.0 ND Filter

Heat Pipe Temp	Unattenuated Signal	Attenuated Signal, OD-1.0	Attenuation Ratio
90° C	0.740 nVs	0.0678 nVs	10.9
120° C	2.035 nVs	0.179 nVs	11.4

Table A.3. Verification of Attenuation Factor of OD-2.0 ND Filter

Heat Pipe Temp	Attenuated Signal, OD-1.0	Attenuated Signal, OD-2.0	Attenuation Ratio
120° C	0.179 nVs	0.0202 nVs	8.9
150° C	0.310 nVs	0.027 nVs	11.4
180° C	0.939 nVs	0.1165 nVs	8.1

The average attenuation factor of the OD-0.5 ND filter was 4.61. For the OD-01 filter, the average ratio was 11.1. Since an unsaturated, unattenuated signal and a detectable, OD-2.0 attenuated signal could not be obtained at the same heat pipe temperature, the OD-2.0 filter was compared to the OD-1.0 filter. The average ratio of the OD-2.0 filter to the OD-1.0 filter was 9.4. Thus, the attenuation factor of the combined OD-2.0 mid-IR ND filter and OD-0.5 absorptive ND filter was $(9.4 \times 11.1) \times 4.61 = 481.5$. This was very close to the assumed value of ~500.

REPORT DOCUMENTATION PAGE					Form Approved OMB No. 0704-0188	
<p>The public reporting burden for this collection of information is estimated to average 1 hour per response, including the time for reviewing instructions, searching existing data sources, gathering and maintaining the data needed, and completing and reviewing the collection of information. Send comments regarding this burden estimate or any other aspect of this collection of information, including suggestions for reducing the burden, to Department of Defense, Washington Headquarters Services, Directorate for Information Operations and Reports (0704-0188), 1215 Jefferson Davis Highway, Suite 1204, Arlington, VA 22202-4302. Respondents should be aware that notwithstanding any other provision of law, no person shall be subject to any penalty for failing to comply with a collection of information if it does not display a currently valid OMB control number.</p> <p>PLEASE DO NOT RETURN YOUR FORM TO THE ABOVE ADDRESS.</p>						
1. REPORT DATE (DD-MM-YYYY) 26-03-2015		2. REPORT TYPE Master's Thesis		3. DATES COVERED (From - To) June 2014 - March 2015		
4. TITLE AND SUBTITLE Scaling of an Optically Pumped Mid-Infrared Rubidium Laser				5a. CONTRACT NUMBER		
				5b. GRANT NUMBER		
				5c. PROGRAM ELEMENT NUMBER		
6. AUTHOR(S) Moran, Paul J, 2d Lt, USAF				5d. PROJECT NUMBER		
				5e. TASK NUMBER		
				5f. WORK UNIT NUMBER		
7. PERFORMING ORGANIZATION NAME(S) AND ADDRESS(ES) Air Force Institute of Technology Graduate School of Engineering and Management (AFIT/ENP) 2950 Hobson Way WPAFB OH 45433-7765				8. PERFORMING ORGANIZATION REPORT NUMBER AFIT-ENP-MS-15-M-104		
9. SPONSORING/MONITORING AGENCY NAME(S) AND ADDRESS(ES) Dr. Harro Ackermann Senior Technical Advisor HEL Joint Technology Office 801 University Blvd. SE, Suite 209 Albuquerque, NM 87106 Email: harro.ackerman@jto.hpc.mil				10. SPONSOR/MONITOR'S ACRONYM(S) HEL-JTO		
				11. SPONSOR/MONITOR'S REPORT NUMBER(S)		
12. DISTRIBUTION/AVAILABILITY STATEMENT DISTRIBUTION STATEMENT A. APPROVED FOR PUBLIC RELEASE; DISTRIBUTION UNLIMITED						
13. SUPPLEMENTARY NOTES This material is declared a work of the U.S. Government and is not subject to copyright protection in the United States						
14. ABSTRACT An optically pumped mid-infrared rubidium (Rb) pulsed laser has been demonstrated in a heat pipe along the $6^2P_{3/2} - 6^2S_{1/2}$ transition at 2.730 μm and the $6^2P_{1/2} - 6^2S_{1/2}$ transition at 2.790 μm . The bleached limit, slope efficiency, and maximum laser output energy of the mid-IR Rb laser have been shown to scale linearly with increasing Rb density, contrary to prior laser demonstrations. A maximum output energy of ~5 nJ per pulse had previously been observed before a rollover occurred in the scaling of output energy with Rb concentration. In this experiment, the maximum laser output energy observed was ~100 nJ, with linear scaling to a Rb concentration of $7 \times 10^{15} \text{ cm}^{-3}$. A maximum slope efficiency of 1.7×10^{-4} was observed. Evidence that only a small percentage (<2%) of the available pump photons were absorbed at a concentration of $2 \times 10^{15} \text{ cm}^{-3}$ and a pump energy of 10 μJ . This indicated that there were 20,000 pump photons per Rb atom at a pump energy of 10 mJ, and that the effective laser efficiency was 0.65 percent or higher. The hyperfine structure and absorption spectral profile of the $5^2S_{1/2} - 6^2P_{1/2}$ and $5^2S_{1/2} - 6^2P_{3/2}$ (blue) pump transitions were studied using a continuous wave (cw) pump source.						
15. SUBJECT TERMS DPAL, Gas Lasers, Rubidium, IR-CM, Mid-IR						
16. SECURITY CLASSIFICATION OF:			17. LIMITATION OF ABSTRACT UU	18. NUMBER OF PAGES 81	19a. NAME OF RESPONSIBLE PERSON Dr. Glen Perram – ENP	
a. REPORT U	b. ABSTRACT U	c. THIS PAGE U			19b. TELEPHONE NUMBER (Include area code) (937) 255-3636 x 4504 glen.perram@afit.edu	